Supplement of Atmos. Chem. Phys., 26, 11339–11354, 2026
https://doi.org/10.5194/acp-26-11339-2026-supplement


Atmospheric Chemistry and Physics
Open Access
EGU

*Supplement of*

# Reaction kinetics and multi-sulfur products formation of sulfur-containing volatile organic compounds with OH radicals

**Xun Rong et al.**

*Correspondence to:* Lei Yao (lei_yao@fudan.edu.cn)

**S1. Vocus-PTR-LToF-MS and nitrate-CI-LToF-MS**

The Vocus-PTR-LToF-MS was employed to monitor the evolution of sulfur-VOCs in our chamber during the oxidation process at a time resolution of 1 s. This instrument detects VOCs mainly through proton-transfer reactions involving hydronium reagent ions and their water-cluster ions, including $H_3O^+$, $H_5O_2^+$, and $H_7O_3^+$. The mass resolution of Vocus-PTR-LToF-MS was ~10,000 at *m/z* 200 Th. The instrument was calibrated with sulfur-VOC standards and background signals were determined by introducing zero air.

The nitrate-CI-LToF-MS was used to measure and identify the oxidation products formed from the reactions of sulfur-VOCs with •OH. This instrument employs $(HNO_3)_n \cdot NO_3^-$ cluster ions to selectively ionize oxidized molecules, demonstrating a resolving power up to 9000 for ions with *m/z* > 200 Th. Mass calibration was performed using $NO_3^-$, $HNO_3 \cdot NO_3$-, and $(HNO_3)_2 \cdot NO_3^-$ ions. For identification of sulfur-containing oxygenated organic molecules (sulfur-OOMs), mass accuracy was maintained below 4 ppm.

**S2. Relative-rate determination of •OH reaction rate constants**

•OH were generated by the photolysis of $O_3/H_2O$ mixtures using a 253 nm UV lamp:

$$O_3 + hv\ (253\ nm) \rightarrow O_2 + O(\ ^1D) \qquad \text{R. (S1)}$$

$$O(\ ^1D) + H_2O \rightarrow 2\bullet OH \qquad \text{R. (S2)}$$

Additional relative-rate experiments were conducted to determine the •OH reaction rate constants of selected sulfur-VOCs using isoprene as the reference compound. The relative-rate method derives the rate constant of a target compound from its simultaneous decay with a reference compound under the same oxidizing conditions, and therefore does not require independent determination of the absolute •OH concentration. In each experiment, a selected sulfur-VOC and isoprene were introduced simultaneously into the chamber at 298±2 K and 1 atm. After dark-loss characterization, the UV lamp was turned on to initiate •OH oxidation. The temporal evolution of both the sulfur-VOC and isoprene was monitored by Vocus-PTR-LToF-MS.

The •OH reaction rate constant of isoprene was taken as $10.00 \times 10^{-11}$ $cm^3$ $molecule^{-1}$ $s^{-1}$ at 298 K, consistent with previous kinetic studies (Iida et al., 2002; Medeiros et al., 2018). The relative-rate equation can be expressed as:

$$ln\left(\frac{[sulfur-VOC]_0}{[sulfur-VOC]_t}\right) = \frac{k_{sulfur-VOC}}{k_{isoprene}} ln\left(\frac{[isoprene]_0}{[isoprene]_t}\right) \qquad \text{Eq. (S1)}$$

where $[\text{sulfur-VOC}]_0$ and $[\text{isoprene}]_0$ are the initial concentrations of the target sulfur-VOC and isoprene after the UV lamp was turned on, respectively; $[\text{sulfur-VOC}]_t$ and $[\text{isoprene}]_t$ are their concentrations at reaction time t; $k_{\text{sulfur-VOC}}$ and kisoprene are the corresponding •OH reaction rate constants. The slope obtained from the linear regression of $\ln([\text{sulfur-VOC}]_0/[\text{sulfur-VOC}]_t)$ against $\ln([\text{isoprene}]_0/[\text{isoprene}]_t)$ is equal to $k_{\text{sulfur-VOC}}/k_{\text{isoprene}}$. Therefore, $k_{\text{sulfur-VOC}}$ was calculated by multiplying the regression slope by $k_{\text{isoprene}}$.

Before the relative-rate analysis, the measured concentrations of sulfur-VOCs and isoprene were corrected for dilution and wall loss. The dilution and wall-loss behavior was evaluated during the dark-loss stage before UV irradiation. The corrected concentrations were then used to calculate the logarithmic depletion of both the target sulfur-VOC and isoprene. This correction minimizes the influence of non-photochemical losses on the derived relative rate constants.

Each relative-rate experiment was conducted in triplicate. The final •OH reaction rate constants reported in Table 2 represent the average values from the replicate experiments, and the uncertainties represent the standard deviations of the triplicate measurements. Representative relative-rate plots are shown in Figure 1.

**S3. Wall and dilution loss correction for relative-rate experiments**

For each relative-rate experiment, a dark-loss stage was conducted before the UV lamp was turned on. During this stage, the temporal changes in the sulfur-VOC and isoprene signals were monitored under the same chamber flow conditions but without photochemical •OH production. The observed dark loss represents the combined influence of chamber dilution, wall loss, and other non-photochemical losses.

The dark-loss rate constants of the target sulfur-VOC and isoprene were determined separately by fitting their concentration decays during the dark-loss stage:

$$ln\left(\frac{[X]_t}{[X]_0}\right) = -k_{dark,X}\,t \qquad \text{Eq. (S2)}$$

where X denotes either the target sulfur-VOC or isoprene, and $k_{dark,X}$ represents the corresponding first-order dark-loss rate constant. After the UV lamp was turned on, the measured concentrations were corrected for dark loss according to:

$$[X]_{corr,t} = [X]_{meas,t} \times \exp(k_{dark,X}\,t) \qquad \text{Eq. (S3)}$$

where $[X]_{meas,t}$ is the measured concentration at reaction time t after UV irradiation, and $[X]_{corr,t}$ is the dark-loss-corrected concentration used in the relative-rate analysis.

This experiment-specific correction was applied independently to both the target sulfur-VOC and isoprene in each relative-rate experiment. Therefore, the relative-rate plots shown in Figure 1 were constructed using loss-corrected logarithmic depletions, $ln([\text{sulfur-VOC}]_0/[\text{sulfur-VOC}]_t)$ and $ln([\text{isoprene}]_0/[\text{isoprene}]_t)$. This procedure minimizes the influence of dilution and wall loss on the derived •OH reaction rate constants.

**S4. Calibration of Vocus-PTR-LToF-MS using standard sulfur-VOCs**

A mixture of calibration gases containing methanethiol, DMS, ethyl methyl sulfide, and DMDS was used to calibrate the Vocus-PTR-LToF-MS for quantifying sulfur-VOCs selected in the chamber experiments and sulfur-VOCs emitted from freshwater algae samples. The original mixing ratios of these four reduced sulfur compounds in the standard mixture were 1.0 ppmv (parts per million by volume)

(Weichuang Gas Ltd., China). To ensure that the calibration was applicable to atmospherically relevant levels of sulfur-VOCs, the standard mixture was diluted with high-purity $N_2$ to pptv levels. As shown in Figure S13, the resulting sensitivities for methanethiol, DMS, ethyl methyl sulfide, and DMDS were 0.61, 0.92, 0.57, and 0.82 cps $pptv^{-1}$, respectively.

For freshwater algae-emitted sulfur-VOCs with available calibration standards or closely related calibrated compounds, the corresponding experimentally determined sensitivities were used. For signals without compound-specific calibrations, proxy sensitivities were assigned based on the available sulfur-VOC calibrations and the number of sulfur atoms in the assigned molecular formulas. The sensitivity assignments used for the 20 sulfur-VOCs are summarized in Table S5. Because Vocus-PTR-LToF-MS measurements constrain molecular formulas rather than isomer-specific structures, and because authentic standards were not available for all detected sulfur-containing signals, the corresponding mixing ratios should be regarded as semi-quantitative apparent values. In particular, isomeric compounds with the same molecular formula, such as DMS and ethanethiol ($C_2H_6S$), cannot be distinguished solely by high-resolution PTR-MS and may exhibit different sensitivities. In addition, uncertainties in proton-transfer reaction rate constants, compound-dependent instrument responses, and potential ionization-related artifacts can further affect the absolute quantification. Therefore, these reported values should be interpreted as semi-quantitative apparent mixing ratios rather than definitive concentrations of individual compounds (Hansel et al., 1995; Krechmer et al., 2018; Yuan et al., 2017).

To assess the potential influence of PTR ionization-related fragmentation, single-component calibration experiments of representative sulfur-VOC standards were examined. The selected compounds covered the major sulfur-VOC classes investigated in this study, including ethanethiol, 1,2-ethanedithiol, DMS, trimethylene sulfide, and DMDS (Figure S14). Potential fragment-like ions were identified based on their synchronous temporal variation with the corresponding parent ions during standard-gas introduction. Because trace impurities or other ionization-related artifacts cannot be completely excluded, these ions are conservatively referred to as fragment-like ions rather than definitive fragments. Fragment-to-parent signal ratios were calculated from stable calibration plateaus, excluding transient periods during concentration switching, and are summarized in Table S4.

Several low-abundance fragment-like ions were observed to vary synchronously with the corresponding parent ions during standard-gas introduction, suggesting possible PTR ionization-related fragmentation. The observed fragment-like ion signals were generally small, with fragment-to-parent ratios ranging from 2.0% to 10.0% for the representative standards examined. These results suggest that the effect of fragment-like ions on the calibration of sulfur-VOCs was minor. Therefore, these fragment-like ions were not taken into account for the calibration of sulfur-VOCs. For concentration calculations, calibrated parent-ion signals were used consistently for standard compounds, and fragment-like ion signals were not added to parent-ion signals to avoid double counting. Because the calibration factors

were derived using the same parent-ion signals used for quantification, the influence of fragmentation on calibrated parent-ion sensitivities was implicitly reflected in the measured sensitivities.

To minimize the potential influence of fragmentation-related artifacts on the interpretation of algae-emission data, the identified fragment-like ion formulas were removed from Figure 4a. Therefore, Figure 4a presents the mass-defect distribution of VOC formulas after excluding the identified fragment-like ion formulas from the representative single-component calibration experiments. The sulfur-VOCs listed for algae emissions should still be interpreted as PTR-MS formula-level signals rather than definitive evidence for unique independently emitted molecular structures. Accordingly, these signals were not used to construct a complete sulfur mass balance. Instead, they were used to characterize the occurrence and relative abundance of sulfur-VOCs emitted from freshwater algae. Figure 4a should therefore be interpreted as a qualitative visualization of normalized PTR-MS signals after excluding identified fragment-like ions, rather than as a concentration-based distribution of individual sulfur-containing compounds.

**S5. Semi-quantification of multi-sulfur products**

Multi-sulfur product concentrations were quantified using Eq. (S4):

$$[\text{multi-sulfur product}] = C \times \frac{(\text{multi-sulfur product})^- + (\text{multi-sulfur product})\cdot NO_3^-}{NO_3^- + HNO_3\cdot NO_3^- + (HNO_3)_2\cdot NO_3^-} \quad \text{Eq. (S4)}$$

where $(\text{multi-sulfur product})^-$, $(\text{multi-sulfur product})\cdot NO_3^-$, $NO_3^-$, $HNO_3\cdot NO_3^-$, and $(HNO_3)_2\cdot NO_3^-$ represent signals of corresponding ions in units of counts per second (cps). For quantification, we assume that multi-sulfur products containing two or more oxygen atoms cluster with $NO_3^-$ at the same collision-limited rate as gaseous $H_2SO_4$. Consequently, the calibration factor $C$ derived for gaseous $H_2SO_4$ is applied to these multi-sulfur species. It should be noted that this assumption may introduce significant uncertainties in the quantification of multi-sulfur species, due to differences in sensitivity between the multi-sulfur species and $H_2SO_4$. The yields reported in Table S3 correspond only to the multi-sulfur products detected by nitrate-CI-LToF-MS and should not be interpreted as total product yields or sulfur mass closure.

**S6. Box-model description for the initial fate of DMS-derived $RO_2$• during DMS + •OH oxidation**

A zero-dimensional photochemical box model was constructed to characterize the initial fate of the DMS-derived $RO_2$• during DMS oxidation under $NO_x$-free chamber conditions. The objective of this simplified model is to estimate the order of magnitude of $HO_2$• and $RO_2$• concentrations and to evaluate the competition between intramolecular H-shift and direct bimolecular loss pathways of the initially formed DMS-derived $RO_2$•, rather than to explicitly predict detailed product distributions or multi-sulfur product yields.

•OH production follows an effective PAM framework in which ozone photolysis generates $O(^1D)$, followed by rapid •OH formation (Table S2) (Atkinson et al., 2004; Lambe et al., 2011). DMS oxidation is initiated by •OH mainly through H-abstraction to form $CH_3SCH_2OO•$, represented here as $RO_2$-MSP (Saunders et al., 2003). The intramolecular H-shift isomerization of $RO_2$-MSP was represented using a first-order rate coefficient of 0.1 $s^{-1}$. This rate coefficient is consistent with reported room-temperature $CH_3SCH_2OO•$ H-shift rate coefficients on the order of 0.1 $s^{-1}$ in recent DMS oxidation studies associated with HPMTF formation (Berndt et al., 2019; Jernigan et al., 2022; Ye et al., 2022).

Rate coefficients for DMS + •OH initiation and key $RO_x$ reactions were adopted from evaluated kinetic mechanisms and literature recommendations where available (Table S2) (Jacob et al., 2023; Jenkin et al., 2015; Saunders et al., 2003). Due to the lack of explicit kinetic data for all individual sulfur-containing $RO_2•$ radicals, $RO_2•$ + $HO_2•$ reactions were represented using generic MCM-type termination rate expressions, while $RO_2•$ + $RO_2•$ cross reactions were parameterized using self-reaction rate constants and a geometric-mean approximation. Therefore, the model should be interpreted as a simplified radical-fate analysis rather than a fully explicit DMS oxidation mechanism.

The modeled $HO_2•$ and total $RO_2•$ concentrations remain below $2.26 \times 10^8$ and $1.56 \times 10^9$ molecules $cm^{-3}$, respectively, during the first 6 min of the simulation (Figure S6). Under these radical concentrations, the initially formed DMS-derived $RO_2$-MSP radical is predicted to undergo efficient H-shift isomerization. On average during 1-6 min, H-shift accounts for 92.7% of the initial fate of $RO_2$-MSP, whereas direct $RO_2$-MSP + $RO_2•$ and $RO_2$-MSP + $HO_2•$ reactions account for 3.8% and 3.6%, respectively (Figure S7). This result indicates that intramolecular H-shift is the dominant competing pathway for the initially formed DMS-derived $RO_2•$ radical under the present chamber conditions, while direct bimolecular reactions of this initial $RO_2•$ radical are minor.

Because this model focuses on the initial fate of $RO_2$-MSP and uses lumped representations of sulfur-containing $RO_2•$ chemistry, it cannot quantitatively separate the contributions of H-migration, $RO_2•$ + $HO_2•$, and different sulfur-$RO_2•$ + $R'O_2•$ pathways to individual multi-sulfur products. Therefore, the model results are used only to constrain the competition between H-shift and direct bimolecular loss of the initially formed DMS-derived $RO_2•$ radical. The detected multi-sulfur products are interpreted as evidence for potential bimolecular chemistry involving sulfur-containing $RO_2•$ radicals under $NO_x$-free conditions, rather than as products formed solely from direct reactions of the initially formed $RO_2$-MSP radical.

Stabilized products formed from $RO_2•$ termination reactions (e.g., ROOH and carbonyl-type products) are treated as inert end products. Because $HO_2•$ regulates $RO_2•$ fate under low-$NO_x$ conditions, the $HO_2•$ self-reaction ($HO_2•$ + $HO_2•$ → $H_2O_2$ + $O_2$) is included as a fundamental $HO_2•$ sink (Atkinson et al., 2004; Lightfoot et al., 1992). A first-order dilution and wall-loss term is applied uniformly to represent chamber losses. Figure S6 shows the simulated DMS, •OH, $HO_2•$, and total $RO_2•$ concentrations over the first 6

min. Figure S7 presents the estimated initial fate of $RO_2$-MSP, including H-shift, $RO_2$-MSP + $RO_2$•, and $RO_2$-MSP + $HO_2$• pathways. The complete reaction set and kinetic parameters are summarized in Table S2.

**S7. Filtration control experiment for freshwater algae samples**

To examine whether the detected sulfur-VOC signals were associated with particulate biological material, a filtration control experiment was conducted using the algae-containing freshwater sample. The sample was filtered using three stacked layers of ordinary qualitative laboratory filter paper, similar to commonly used Grade 1 qualitative cellulose filter papers for routine liquid clarification, and the filtration procedure was repeated three times to enhance the removal of visible algal particles and particulate biological material. Such qualitative filter papers are typically designed for clarification of suspensions and have nominal particle-retention sizes on the order of several to tens of micrometers. Therefore, the filtration treatment should be interpreted as a particulate-removal procedure rather than size-resolved membrane filtration, sterile filtration, or a method to completely remove bacteria and dissolved sulfur precursors.

Photographs of the filtration process and the samples before and after filtration are shown in Figure S16. After three rounds of filtration, the green algal suspension became nearly clear, indicating effective removal of most visible algal biomass. The corresponding sulfur-VOCs measured before and after filtration are compared in Figure S17. The filtered sample was used as a control to evaluate the association between the sulfur-VOC signals and the particulate biological fraction.

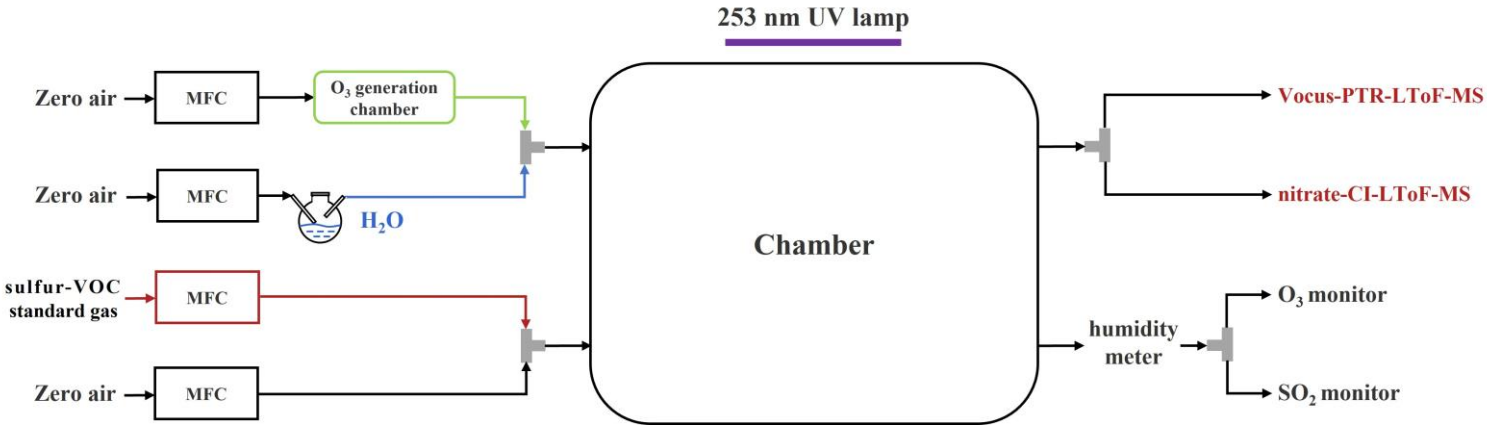


**Figure S1.** Schematic diagram of the chamber setup and instruments used in the laboratory experiments. MFC: mass flow controller.

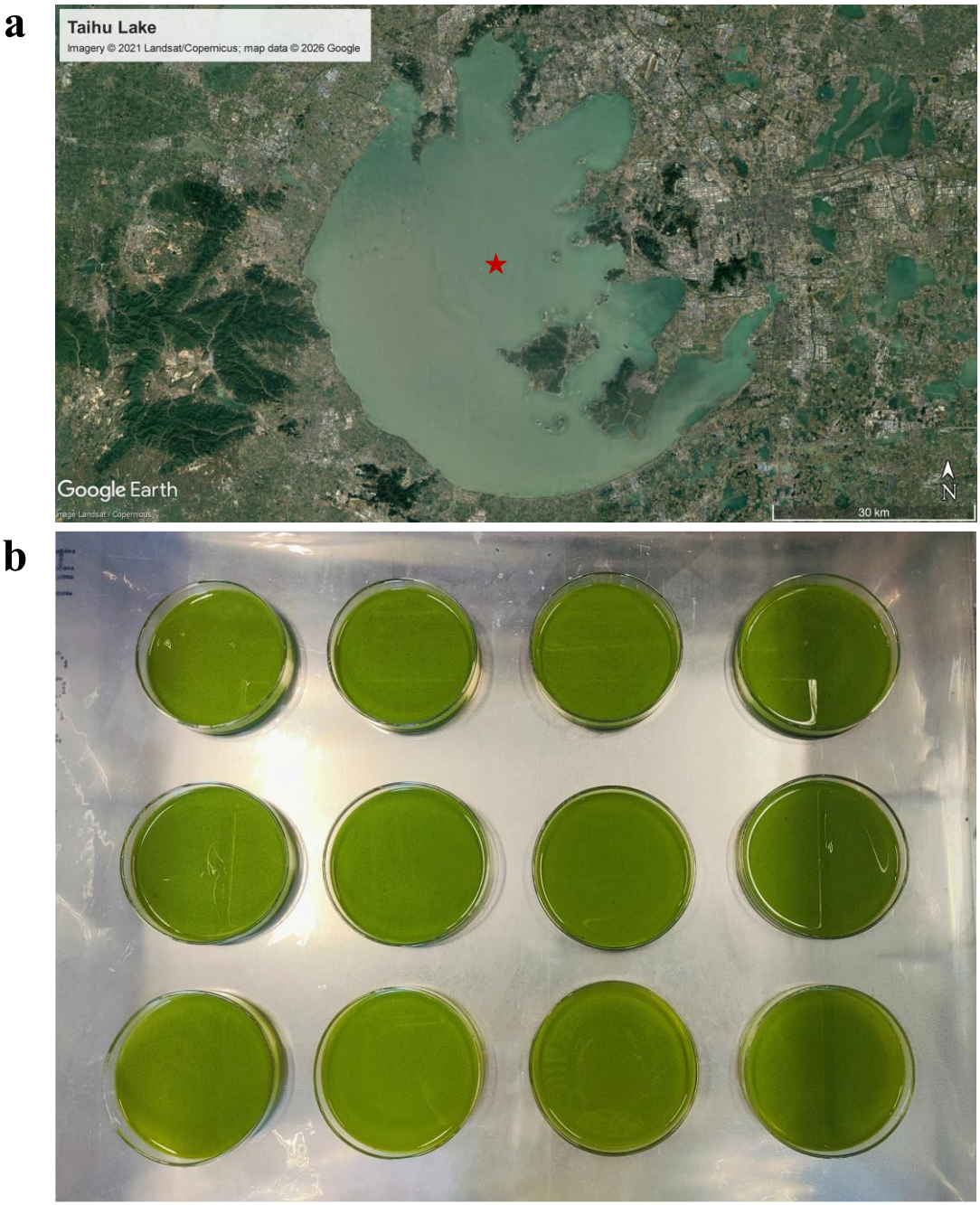


**Figure S2.** (a) Satellite image of Taihu Lake, China. The red star indicates the central lake region. The scale bar indicates distance in kilometers. Imagery © 2021 Landsat/Copernicus; map data © 2026 Google. (b) Photograph of the untreated algae-containing freshwater sample distributed among 12 Petri dishes in the chamber.

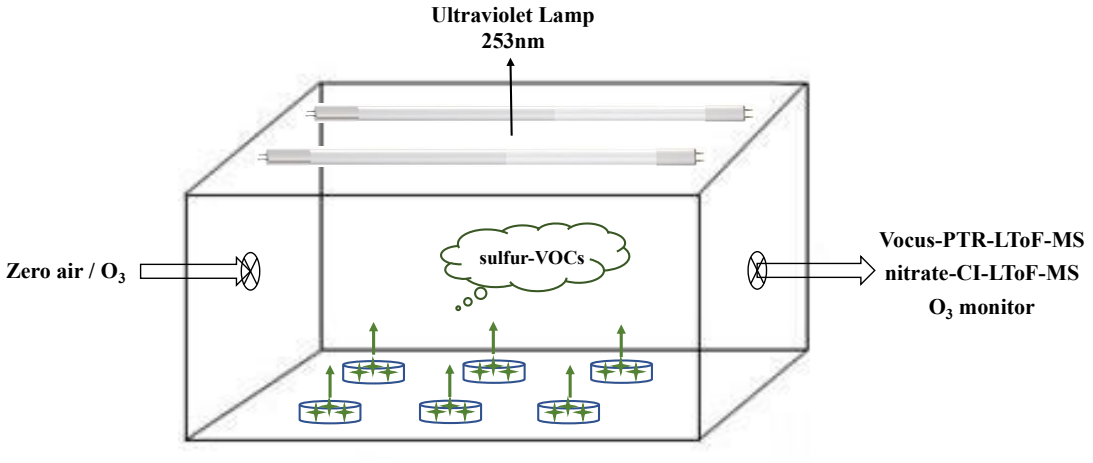


202

203 **Figure S3.** Schematic diagram of the chamber used for the characterization and oxidation of VOCs
204 emitted from the algae-containing freshwater sample. The chamber dimensions were 100 cm (L) × 86
205 cm (W) × 62 cm (H), corresponding to a volume of 533 L.

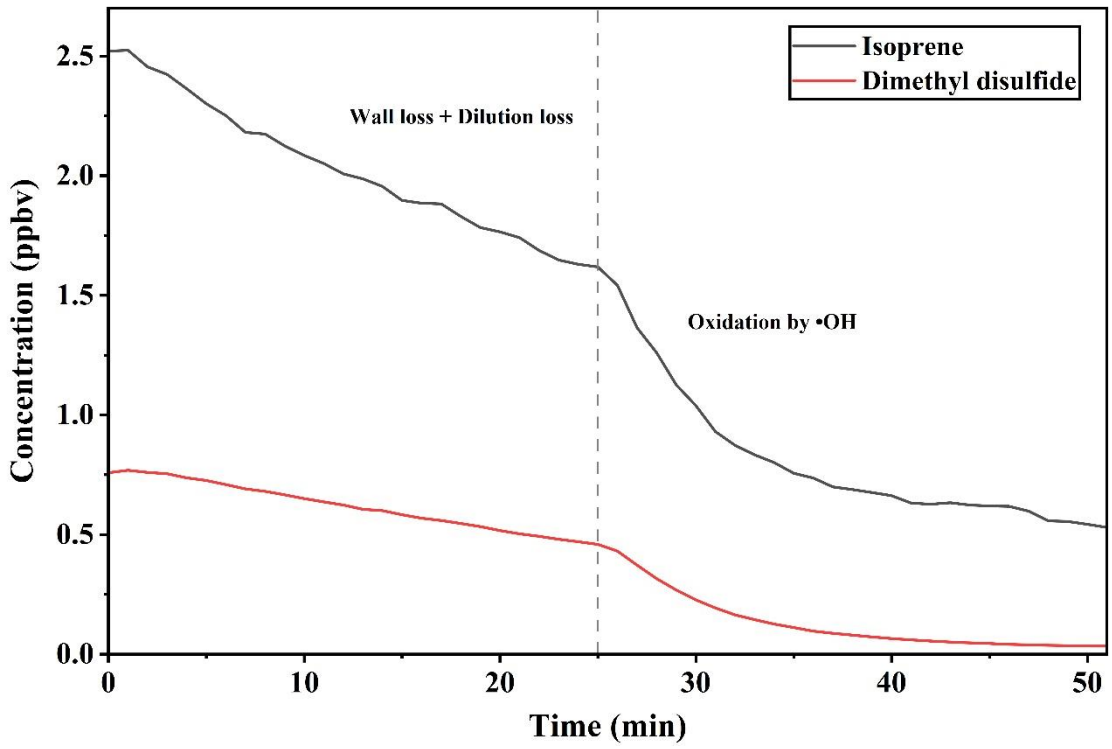


**Figure S4.** Representative time series of isoprene and dimethyl disulfide during an additional relative-rate experiment.

209

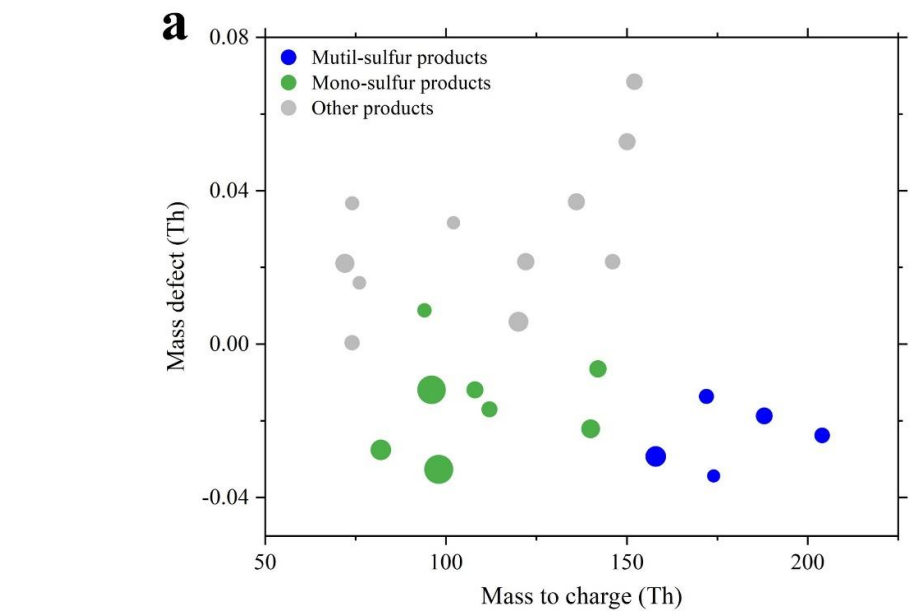
a
Mutil-sulfur products
Mono-sulfur products
Other products
Mass defect (Th)
Mass to charge (Th)
0.08
0.04
0.00
-0.04
50
100
150
200

210

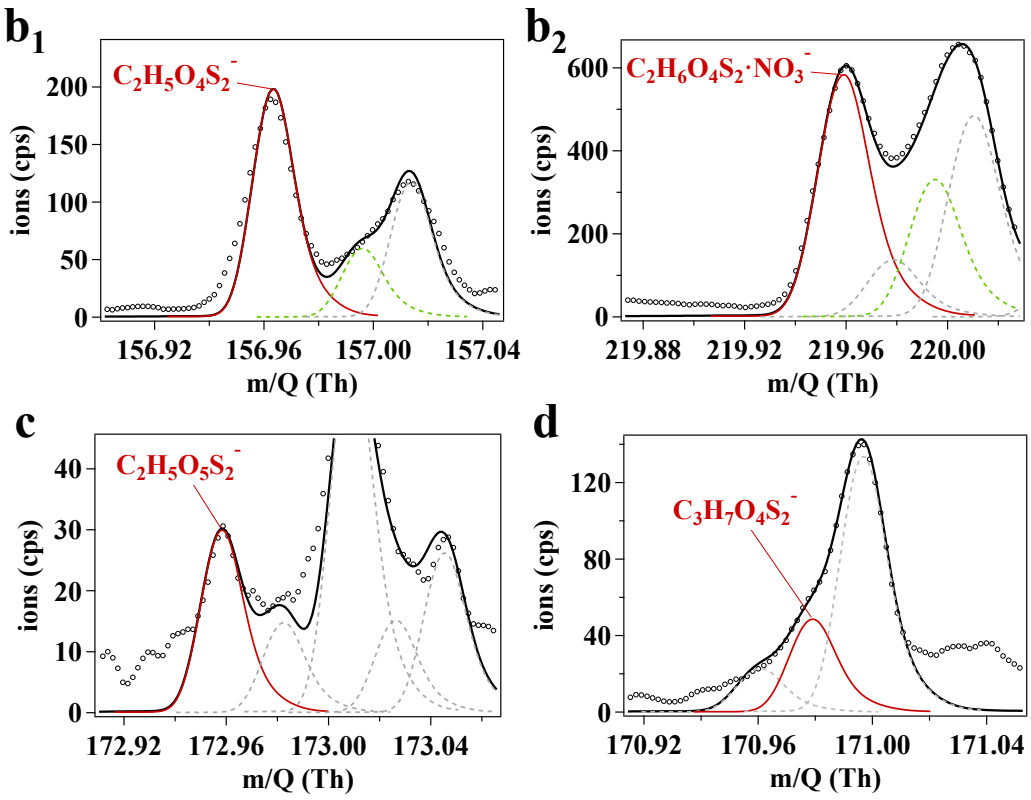
b1
C2H5O4S2-
ions (cps)
m/Q (Th)
156.92
156.96
157.00
157.04
b2
C2H6O4S2·NO3-
219.88
219.92
219.96
220.00
c
C2H5O5S2-
172.92
172.96
173.00
173.04
d
C3H7O4S2-
170.92
170.96
171.00
171.04

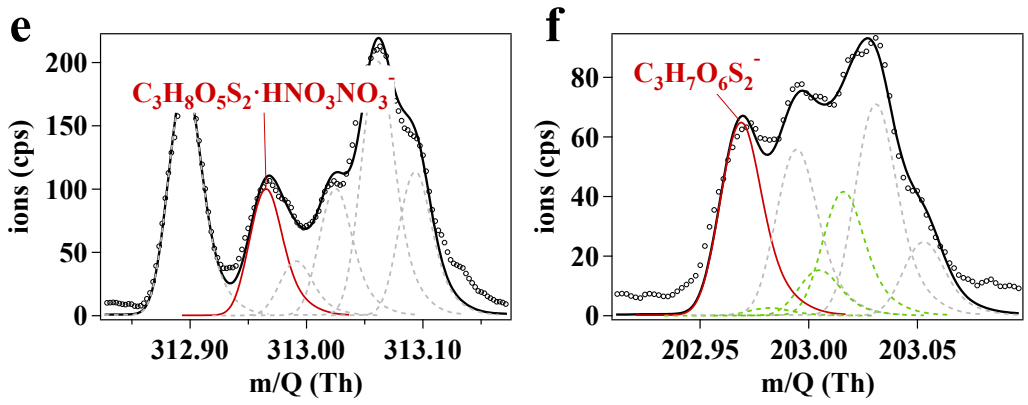


211

212 **Figure S5.** (a) Mass defect plot of reaction products formed from the •OH-initiated oxidation of DMS
213 detected by nitrate-CI-LToF-MS. Blue markers denote multi-sulfur products, green markers indicate
214 mono-sulfur products, and gray markers represent other products. (b-f) High-resolution peak fitting plots
215 of the identified multi-sulfur products.

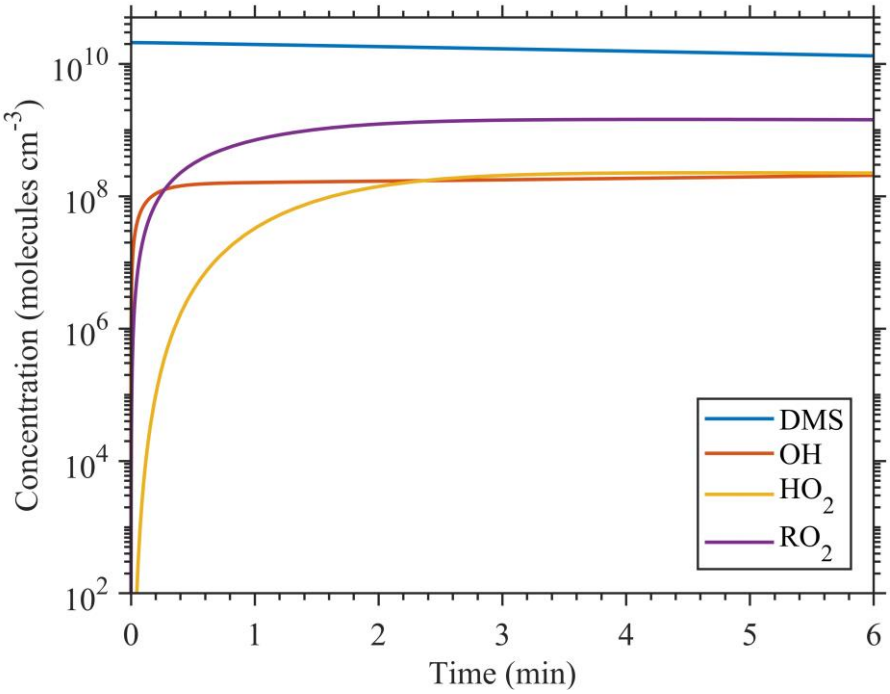


**Figure S6.** Time series of simulated DMS, •OH, $HO_2$•, and total sulfur-containing $RO_2$• concentrations in the chamber under $NO_x$-free conditions (Exp. 10 in Table 1). The simplified box model represents •OH-initiated DMS oxidation over the first 6 min of the experiment and was used to estimate the order of magnitude of $HO_2$• and $RO_2$• concentrations for evaluating $RO_2$• fate under the present chamber conditions.

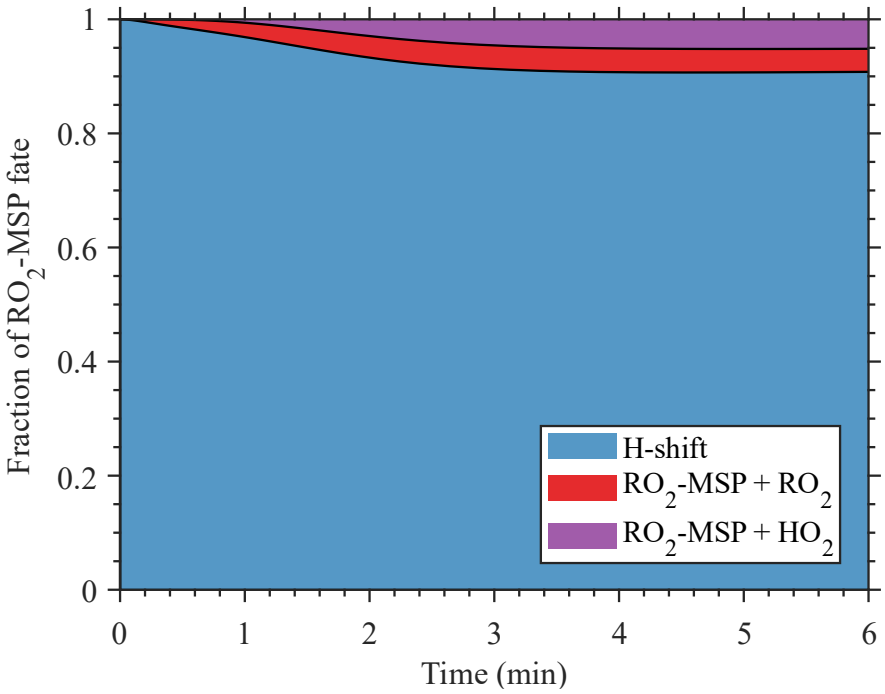


**Figure S7.** Simulated initial fate of the DMS-derived $RO_2$-MSP radical during DMS oxidation under NOx-free conditions (Exp. 10 in Table 1). The pathways include intramolecular H-shift, $RO_2$-MSP + $RO_2$•, and $RO_2$-MSP + $HO_2$• reactions. H-shift was represented using a first-order rate coefficient of 0.1 $s^{-1}$. The results show that H-shift dominates the initial fate of $RO_2$-MSP under the present chamber conditions.

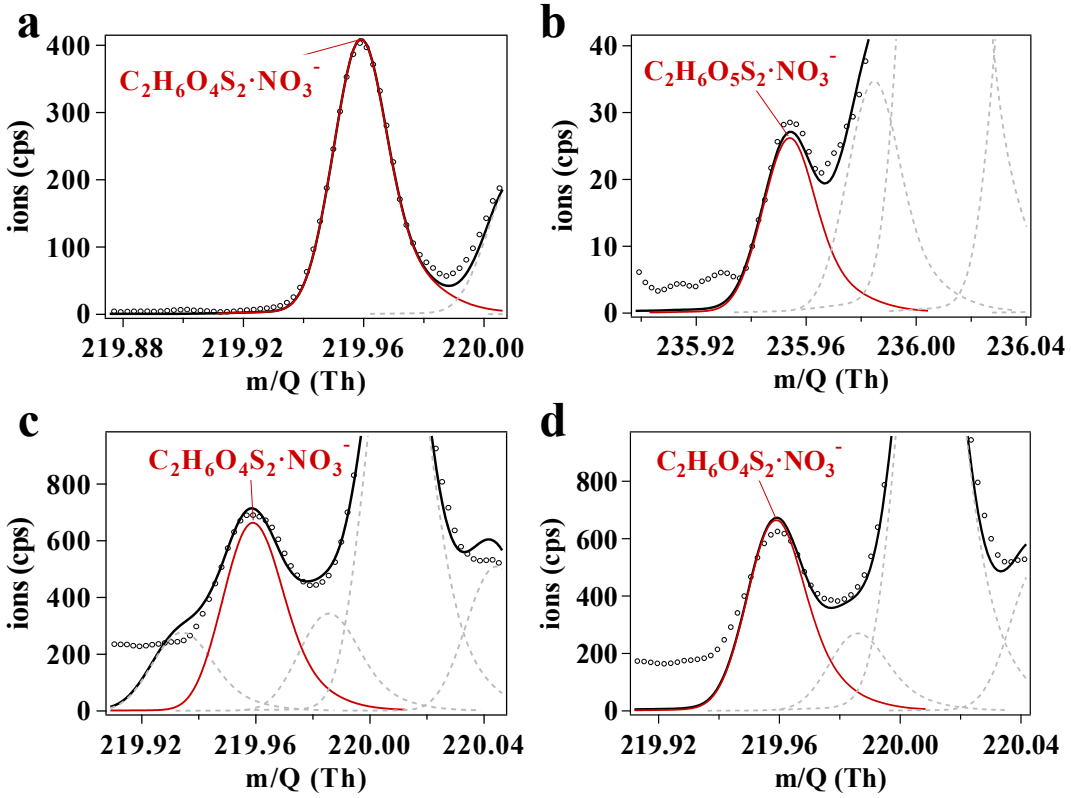


**Figure S8.** High-resolution peak fitting plots of multi-sulfur products formed from the •OH-initiated oxidation of sulfides: $CH_3SCH_2CH_3$ (panels a-b), $CH_3SCH_2SCH_3$ (panel c) and $CH_3S_2CH_3$ (panel d).

231

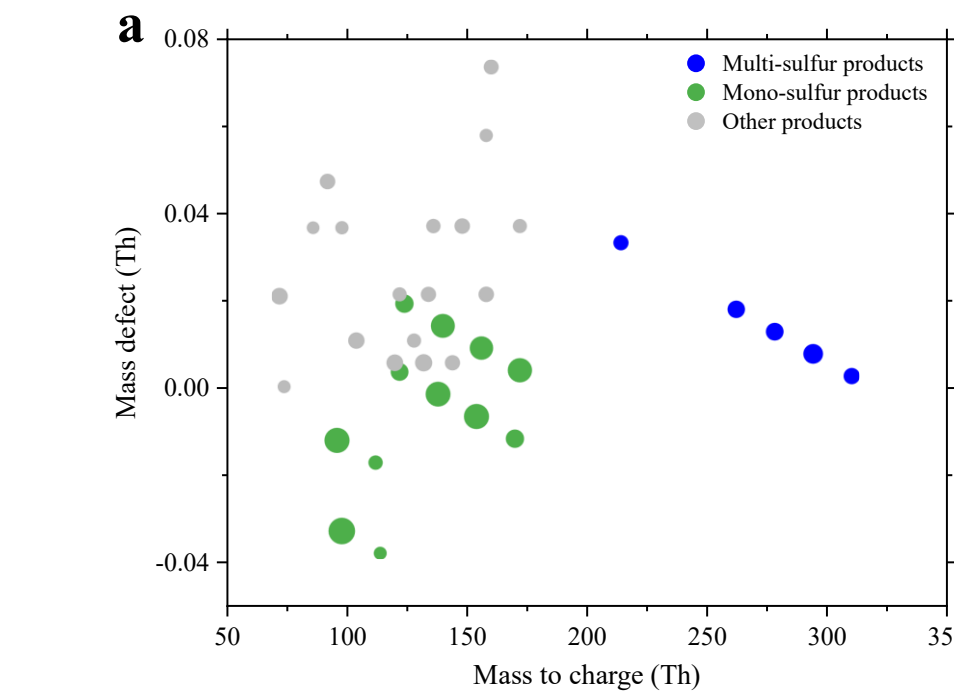
a
Multi-sulfur products
Mono-sulfur products
Other products
Mass defect (Th)
Mass to charge (Th)
0.08
0.04
0.00
-0.04
50
100
150
200
250
300
35

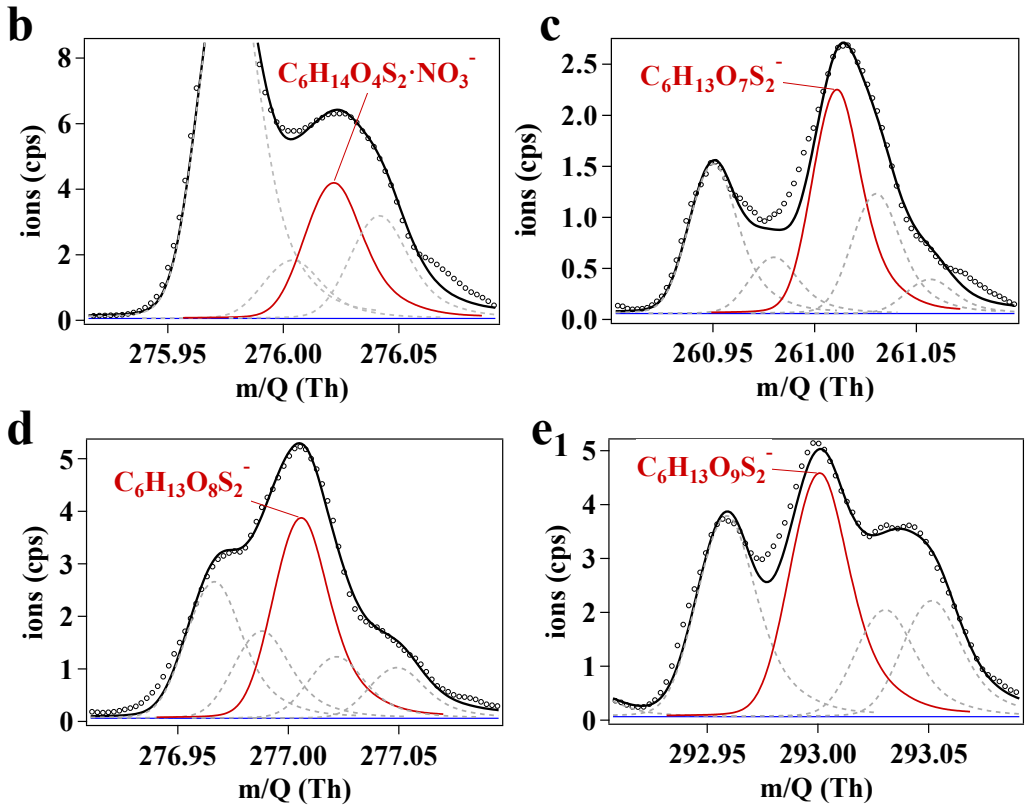
b
$C_6H_{14}O_4S_2 \cdot NO_3^-$
ions (cps)
m/Q (Th)
c
$C_6H_{13}O_7S_2^-$
d
$C_6H_{13}O_8S_2^-$
e1
$C_6H_{13}O_9S_2^-$

232

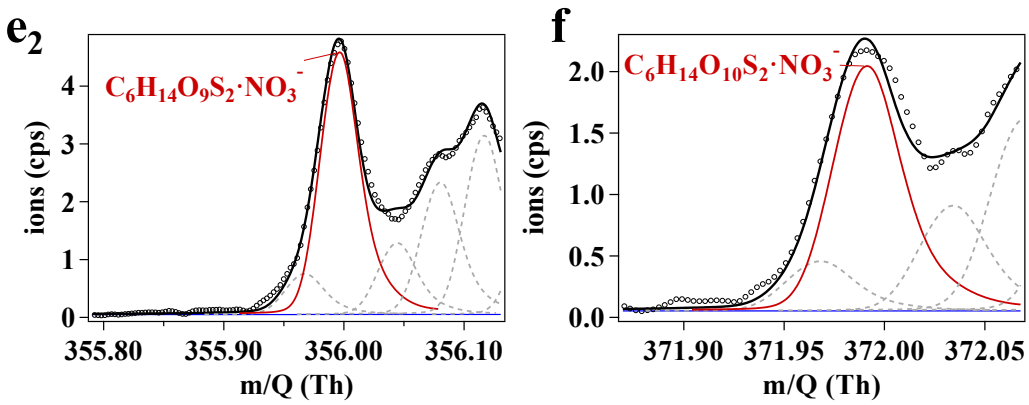


233

234 **Figure S9.** (a) Mass defect plot of reaction products formed from the •OH-initiated oxidation of
235 $HS(CH_2)_3SH$ detected by nitrate-CI-LToF-MS. Blue markers denote multi-sulfur products, green markers
236 indicate mono-sulfur products, and gray markers represent other products. (b-f) High-resolution peak
237 fitting plots of the identified multi-sulfur products.

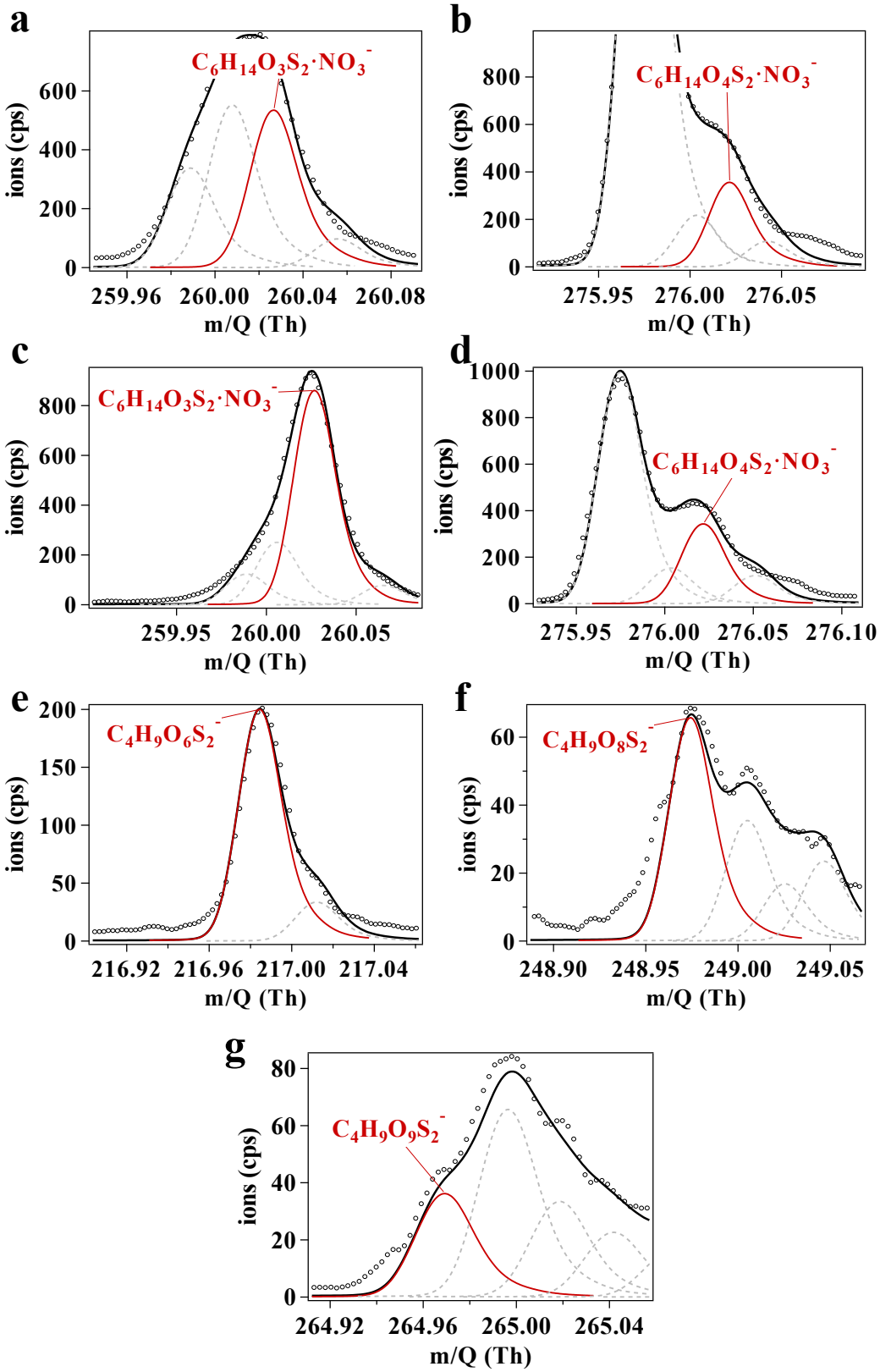


**Figure S10.** High-resolution peak fitting plots of multi-sulfur products formed from the •OH-initiated oxidation of $CH_3(CH_2)_2SH$ (panels a-b), $(CH_3)_2CHSH$ (panels c-d) and $HS(CH_2)_2SH$ (panels e-g).

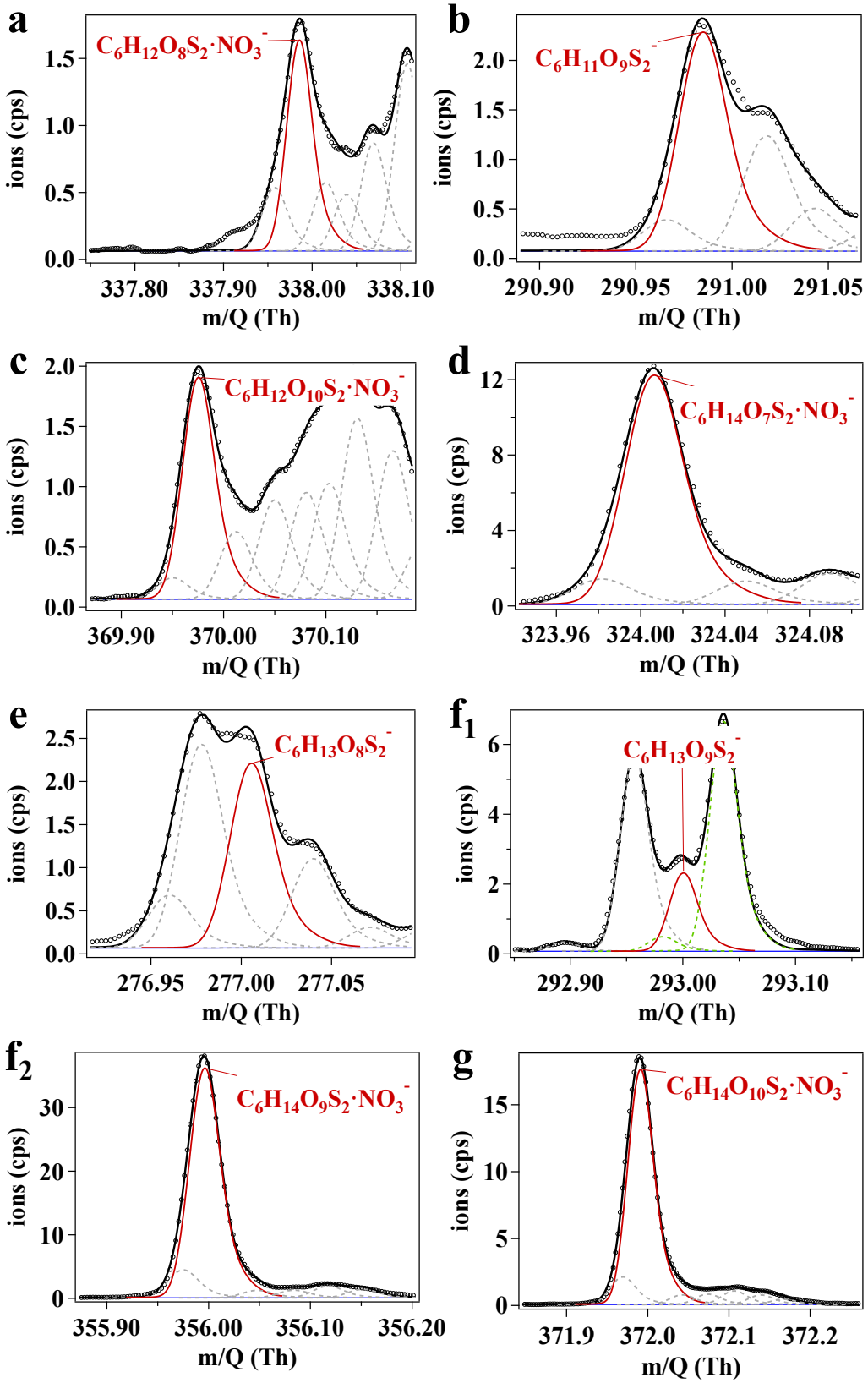


**Figure S11.** High-resolution peak fitting plots of multi-sulfur products formed from the •OH-initiated oxidation of cyclic sulfide (trimethylene sulfide, $C_3H_6S$).

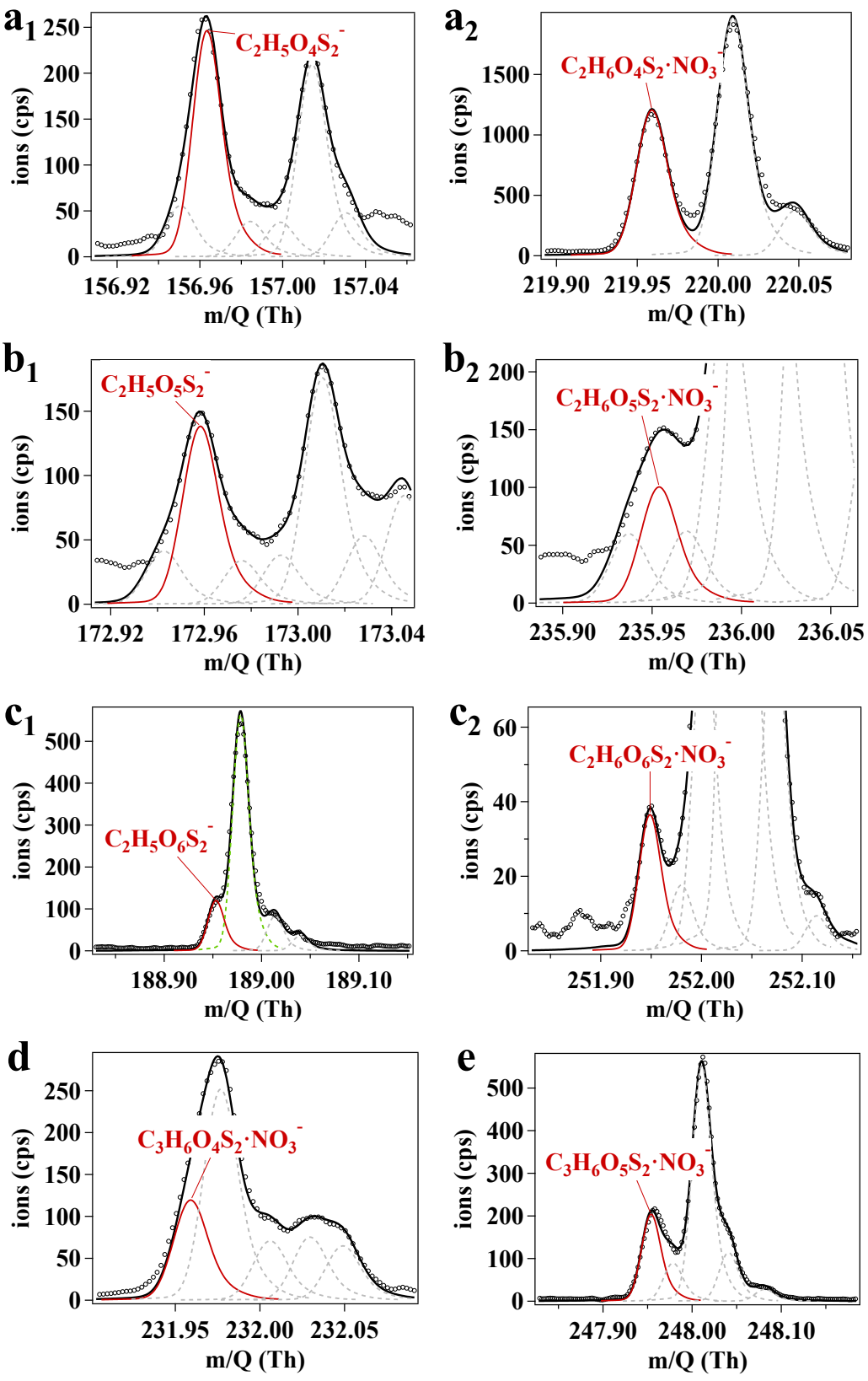
a1
C2H5O4S2-
ions (cps)
m/Q (Th)
a2
C2H6O4S2·NO3-
b1
C2H5O5S2-
b2
C2H6O5S2·NO3-
c1
C2H5O6S2-
c2
C2H6O6S2·NO3-
d
C3H6O4S2·NO3-
e
C3H6O5S2·NO3-

248

249

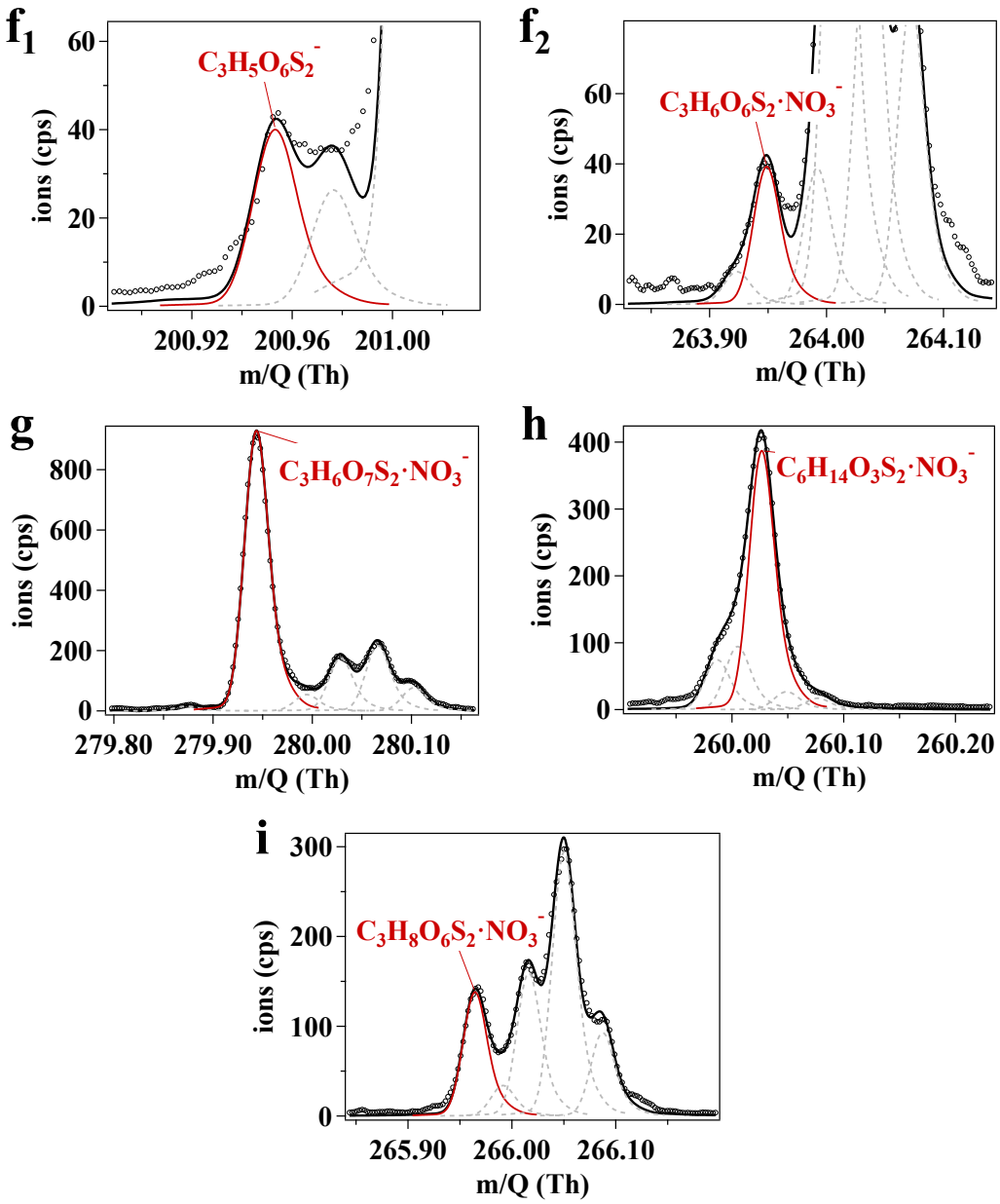


**Figure S12.** High-resolution peak fitting plots of multi-sulfur products formed from the •OH-initiated oxidation of cyclic sulfide (1,3-dithiolane, $C_3H_6S_2$).

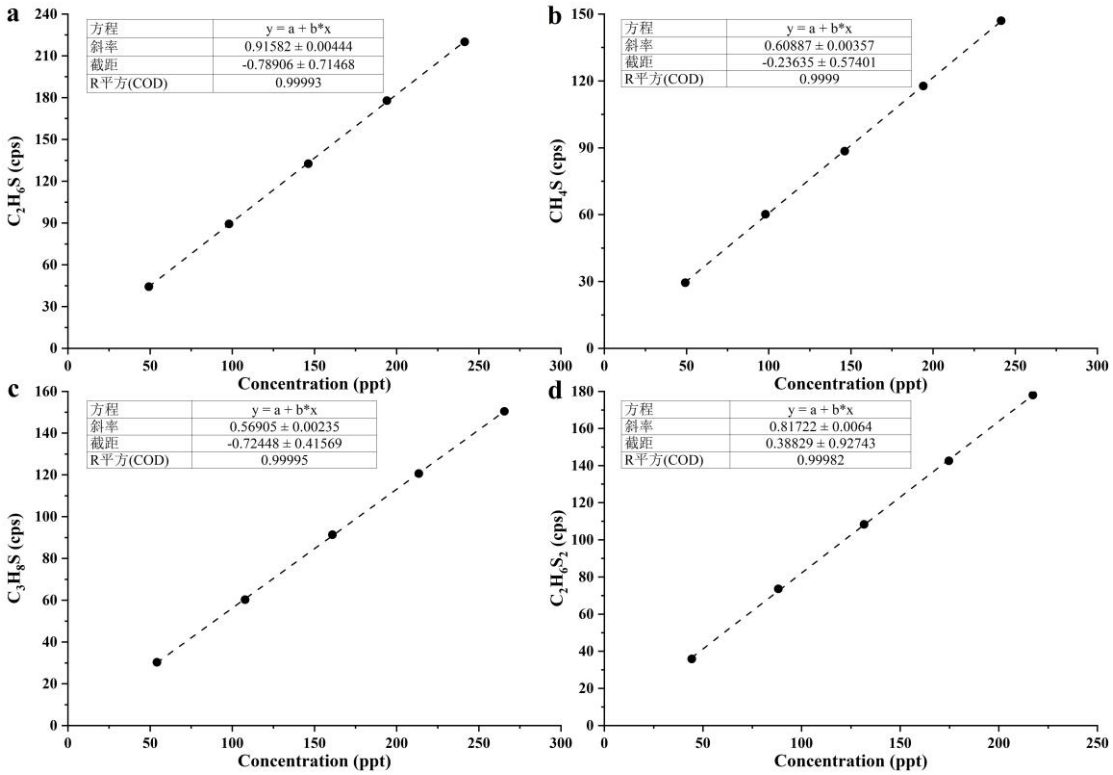


**Figure S13.** Calibration curves relating instrument signal (cps) to standard mixing ratio (ppt) for the target sulfur-VOCs measured by Vocus-PTR-LToF-MS, including (a) $C_2H_6S$, (b) $CH_4S$, (c) $C_3H_8S$, and (d) $C_2H_6S_2$. Dashed lines represent linear least-squares fits.

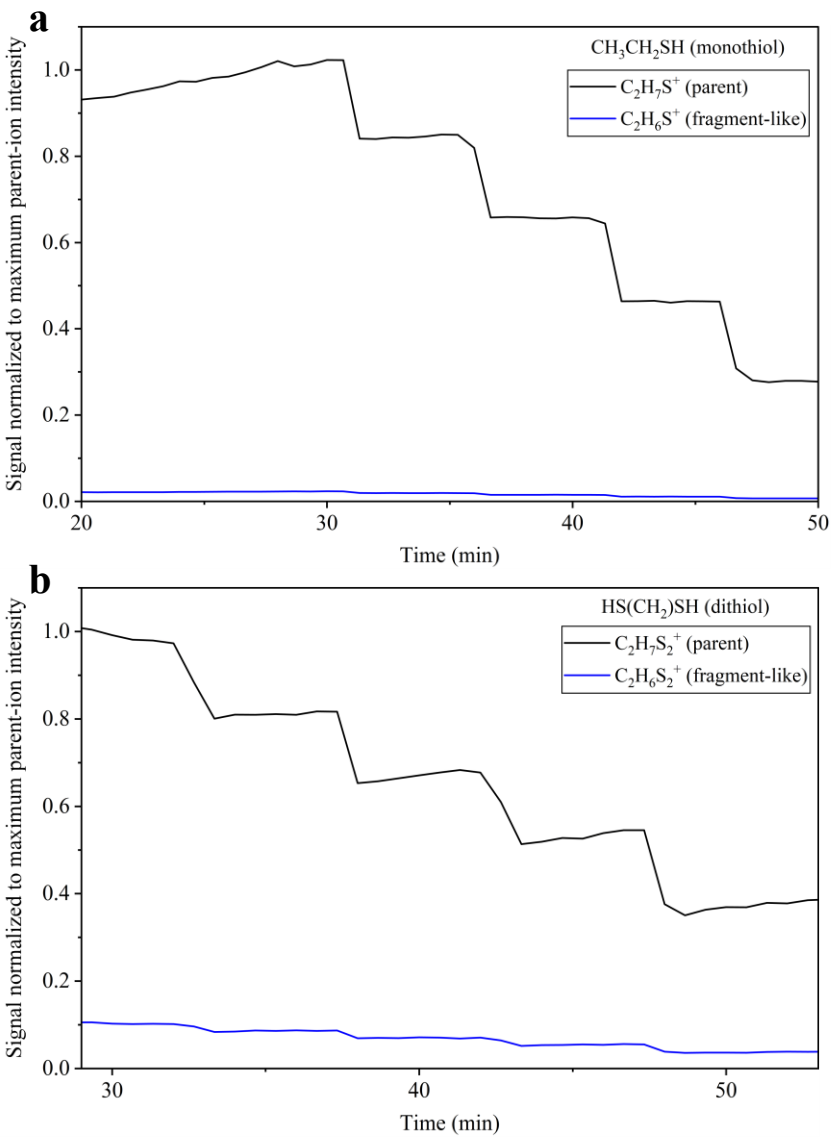
a
CH3CH2SH (monothiol)
C2H7S+ (parent)
C2H6S+ (fragment-like)
Signal normalized to maximum parent-ion intensity
Time (min)
b
HS(CH2)SH (dithiol)
C2H7S2+ (parent)
C2H6S2+ (fragment-like)
Signal normalized to maximum parent-ion intensity
Time (min)
c
CH3SCH3 (acyclic sulfide)
C2H7S+ (parent)
C2H6S+ (fragment-like)
Signal normalized to maximum parent-ion intensity
Time (min)

257

258

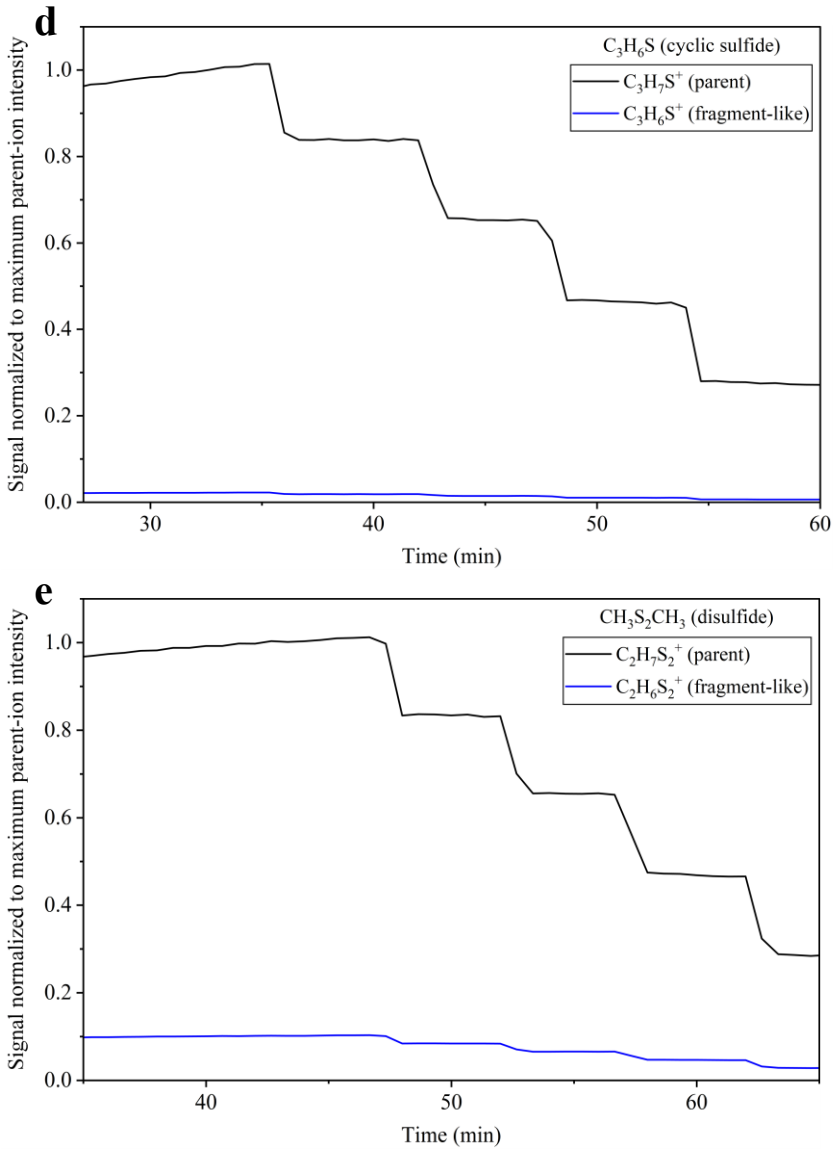


**Figure S14.** Time series of selected parent ions and fragment-like ions observed during single-component calibration experiments of representative sulfur-VOCs by Vocus-PTR-LToF-MS. The representative sulfur-VOC compounds include (a) ethanethiol ($CH_3CH_2SH$), representing monothiols; (b) 1,2-ethanedithiol ($HS(CH_2)_2SH$), representing dithiols; (c) dimethyl sulfide (DMS, $CH_3SCH_3$), representing acyclic sulfides; (d) trimethylene sulfide ($C_3H_6S$), representing cyclic sulfides; and (e) dimethyl disulfide (DMDS, $CH_3S_2CH_3$), representing disulfides. Signals in each panel were normalized to the maximum parent-ion intensity of the corresponding precursor during the calibration sequence.

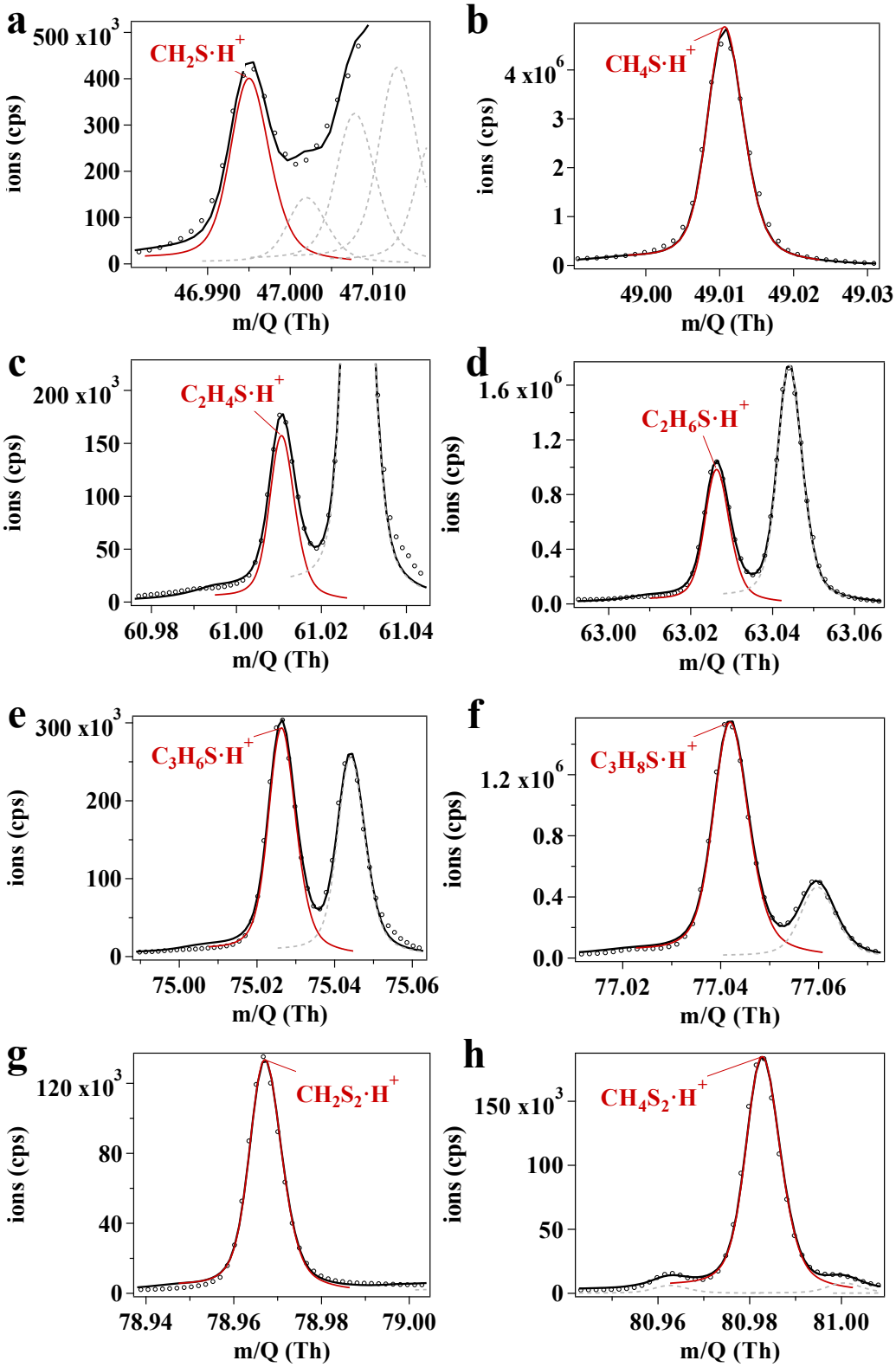
a
500 x10^3
400
300
200
100
0
ions (cps)
CH2S·H+
46.990
47.000
47.010
m/Q (Th)
b
4 x10^6
3
2
1
0
ions (cps)
CH4S·H+
49.00
49.01
49.02
49.03
m/Q (Th)
c
200 x10^3
150
100
50
0
ions (cps)
C2H4S·H+
60.98
61.00
61.02
61.04
m/Q (Th)
d
1.6 x10^6
1.2
0.8
0.4
0.0
ions (cps)
C2H6S·H+
63.00
63.02
63.04
63.06
m/Q (Th)
e
300 x10^3
200
100
0
ions (cps)
C3H6S·H+
75.00
75.02
75.04
75.06
m/Q (Th)
f
1.2 x10^6
0.8
0.4
0.0
ions (cps)
C3H8S·H+
77.02
77.04
77.06
m/Q (Th)
g
120 x10^3
80
40
0
ions (cps)
CH2S2·H+
78.94
78.96
78.98
79.00
m/Q (Th)
h
150 x10^3
100
50
0
ions (cps)
CH4S2·H+
80.96
80.98
81.00
m/Q (Th)

267

268

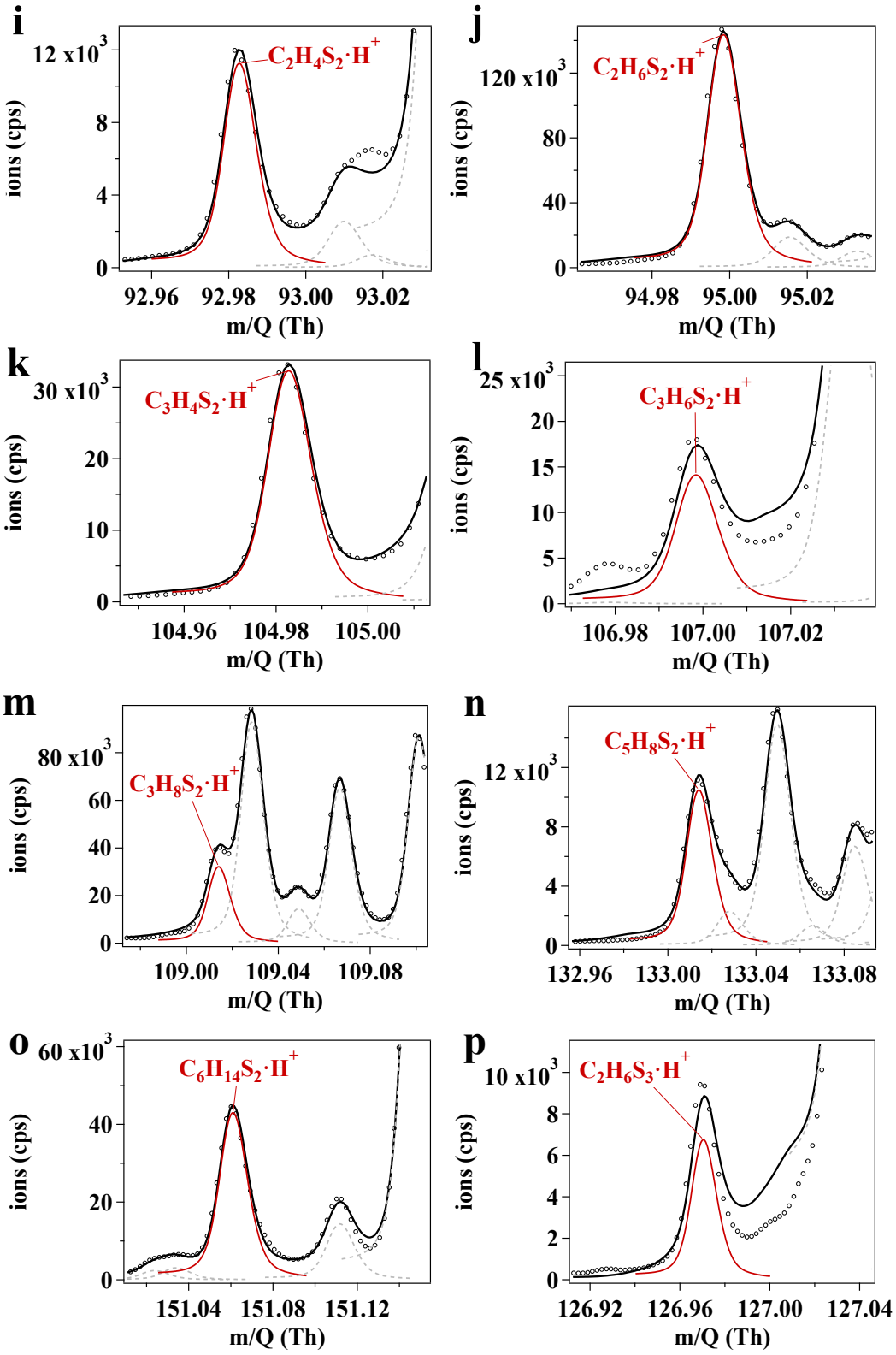
i
12 x10^3
8
4
0
ions (cps)
C2H4S2·H+
92.96
92.98
93.00
93.02
m/Q (Th)
j
120 x10^3
80
40
0
ions (cps)
C2H6S2·H+
94.98
95.00
95.02
m/Q (Th)
k
30 x10^3
20
10
0
ions (cps)
C3H4S2·H+
104.96
104.98
105.00
m/Q (Th)
l
25 x10^3
20
15
10
5
0
ions (cps)
C3H6S2·H+
106.98
107.00
107.02
m/Q (Th)
m
80 x10^3
60
40
20
0
ions (cps)
C3H8S2·H+
109.00
109.04
109.08
m/Q (Th)
n
12 x10^3
8
4
0
ions (cps)
C5H8S2·H+
132.96
133.00
133.04
133.08
m/Q (Th)
o
60 x10^3
40
20
0
ions (cps)
C6H14S2·H+
151.04
151.08
151.12
m/Q (Th)
p
10 x10^3
8
6
4
2
0
ions (cps)
C2H6S3·H+
126.92
126.96
127.00
127.04
m/Q (Th)

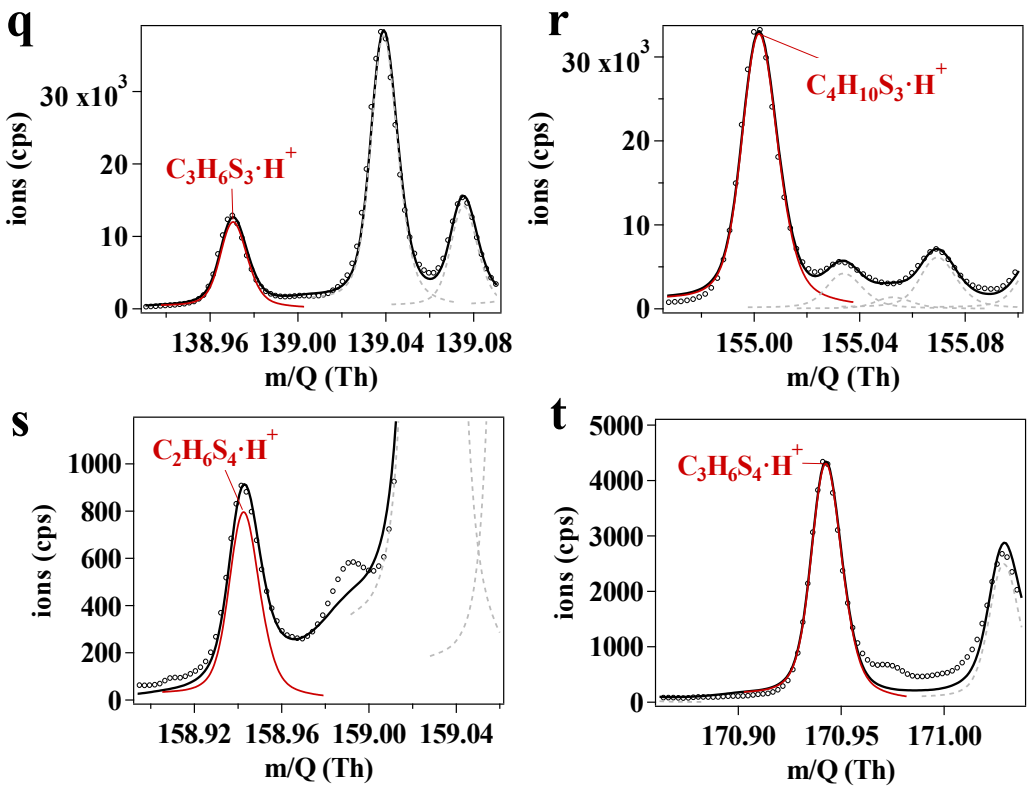


271

272 **Figure S15.** (a-t) High-resolution peak fitting plots of 20 sulfur-VOCs detected from the algae-containing

273 freshwater sample by Vocus-PTR-LToF-MS.

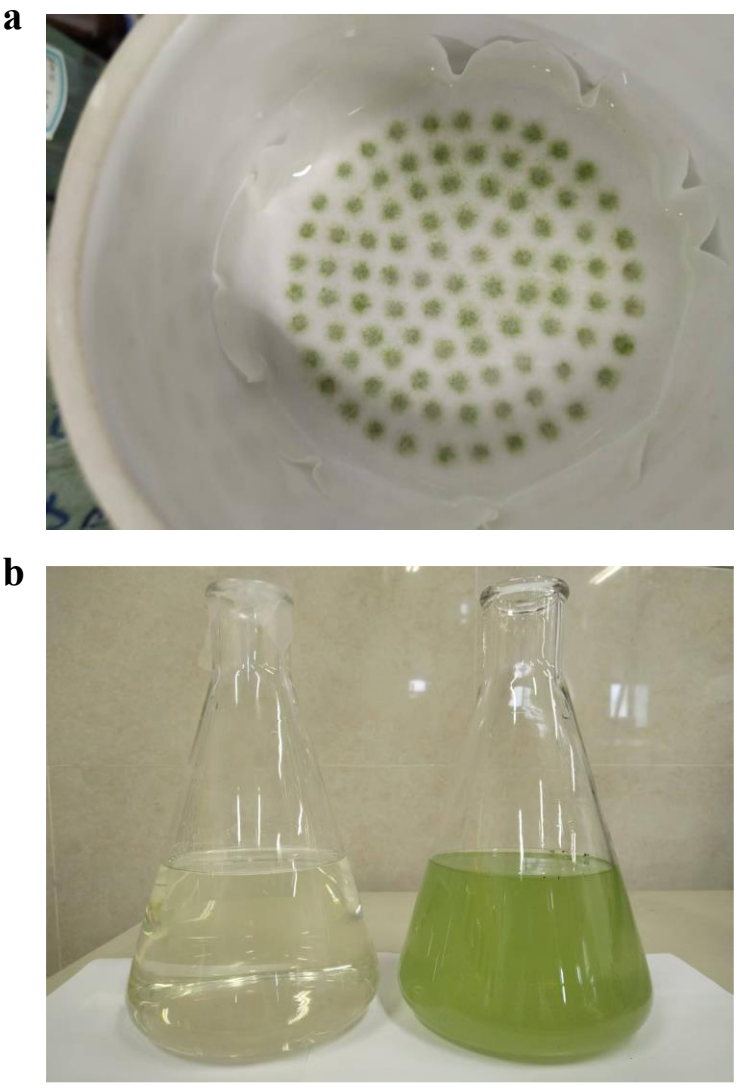


**Figure S16.** Photographs illustrating the filtration control experiment for freshwater algae samples. (a) Algal particles retained on stacked laboratory filter papers during repeated filtration. (b) Visual comparison between the sample after three rounds of filtration (left) and the original algae-containing freshwater sample (right). The filtration treatment effectively removed most visible algal biomass but was not intended to sterilize the sample or completely remove bacteria and dissolved sulfur precursors.

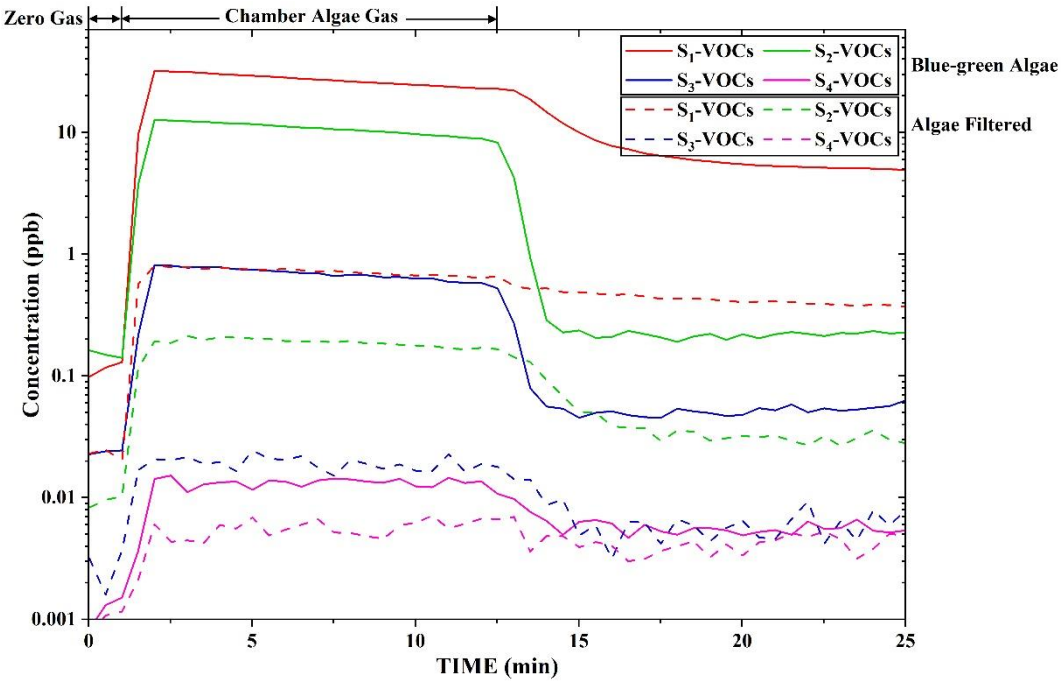


**Figure S17.** Comparison of semi-quantitative mixing ratios of sulfur-VOCs measured before and after repeated filtration of freshwater algae samples. The sulfur-containing signals are classified into four groups ($S_1$-$S_4$) according to the number of sulfur atoms in their assigned molecular formulas.

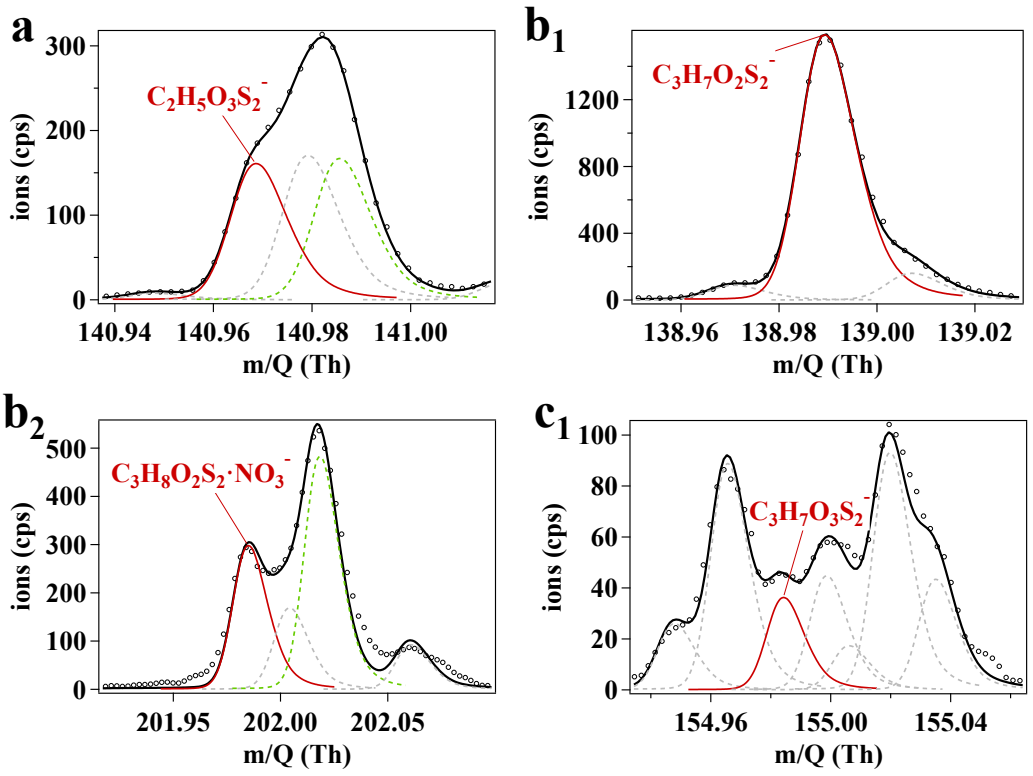
a
$C_2H_5O_3S_2^-$
ions (cps)
m/Q (Th)
b1
$C_3H_7O_2S_2^-$
b2
$C_3H_8O_2S_2 \cdot NO_3^-$
c1
$C_3H_7O_3S_2^-$
c2
$C_3H_8O_3S_2 \cdot NO_3^-$
d
$C_3H_7O_2S_3^-$
e
$C_3H_8O_3S_3 \cdot NO_3^-$
f
$C_4H_9O_2S_2^-$

284

285

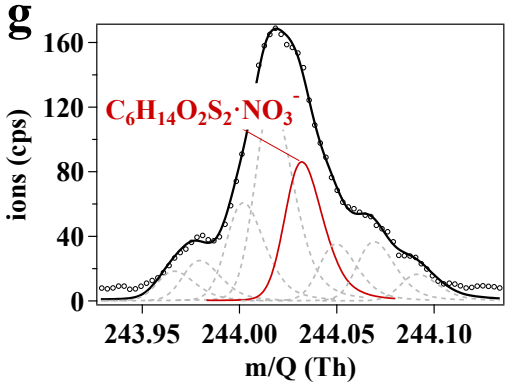


286

287 **Figure S18.** High-resolution peak fitting plots of 7 multi-sulfur products detected by nitrate-CI-LToF-
288 MS in the freshwater algae chamber experiments, whose molecular formulas could be deduced from
289 sulfur-VOCs chamber simulation experiments.

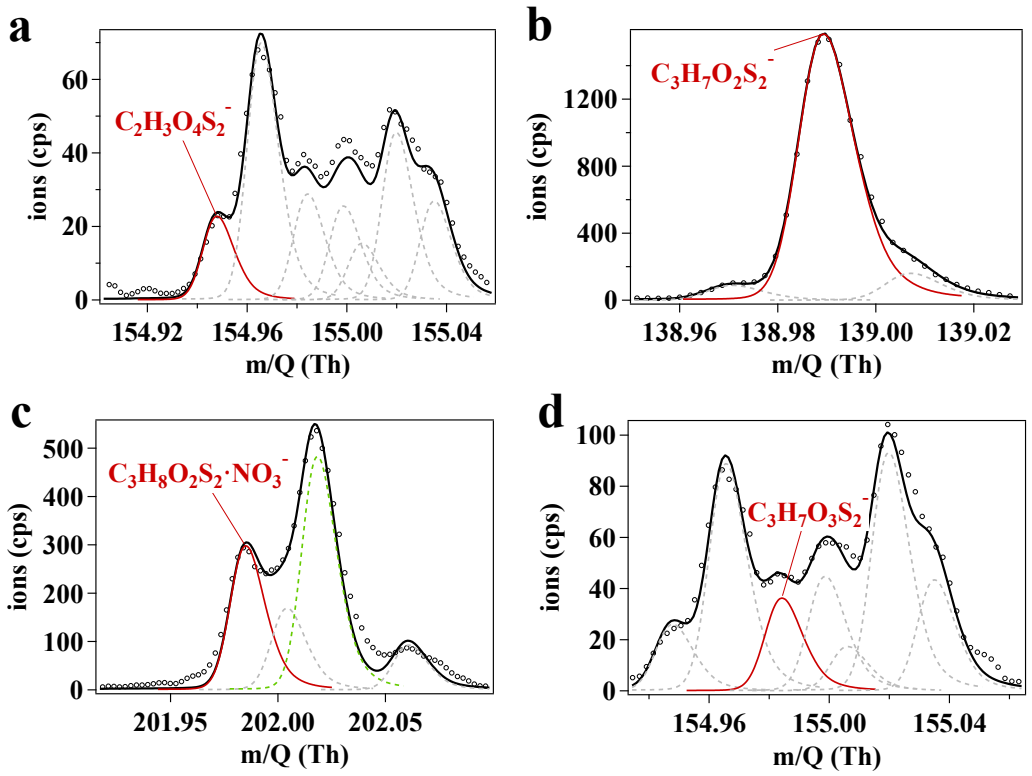


290

291 **Figure S19.** High-resolution peak fitting plots of 4 multi-sulfur products detected by nitrate-CI-LToF-
292 MS in the freshwater algae chamber experiments, whose molecular formulas cannot be deduced from
293 sulfur-VOCs chamber simulation experiments.

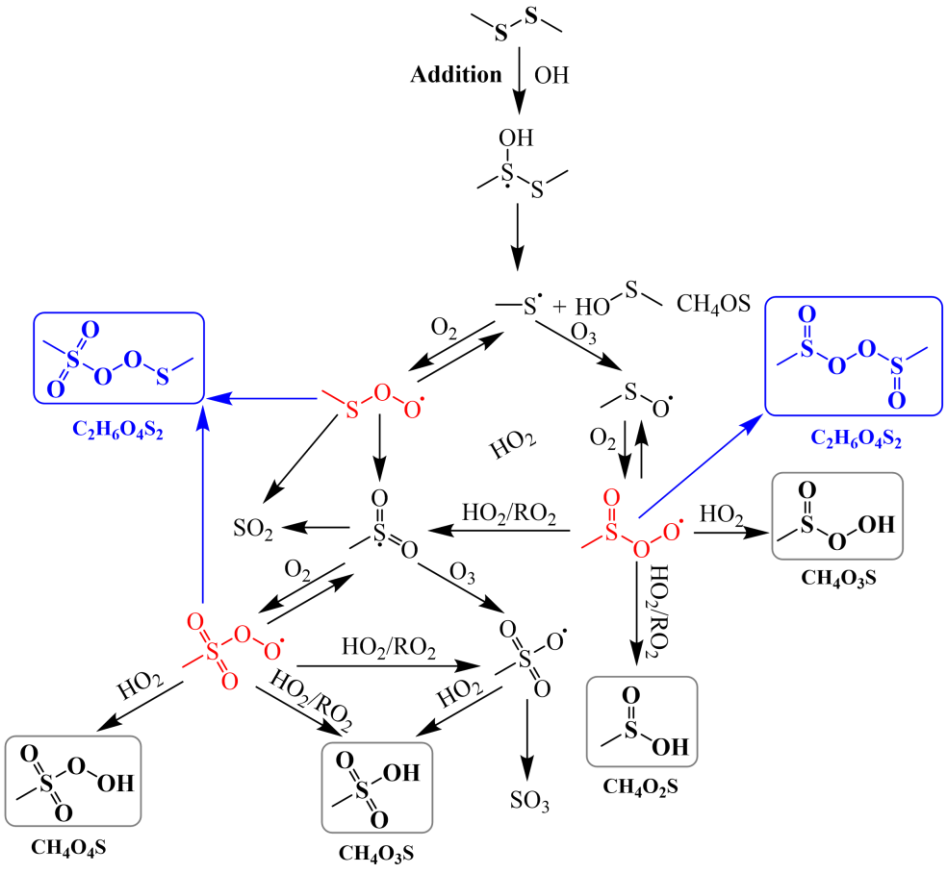


**Scheme S1.** Scheme of the reaction pathways of DMDS with •OH.

297 **Table S1.** Specifications of sulfur-VOCs investigated in our study.

| Serial number | Reagent name | CAS number | Physical state | Brand owner | Product number | Purity |
|---|---|---|---|---|---|---|
| 1 | ethanethiol | 75-08-1 | liquid | Sigma-Aldrich | E3708 | 97% |
| 2 | 1-propanethiol | 107-03-9 | liquid | Sigma-Aldrich | P50757 | 99% |
| 3 | 2-propanethiol | 75-33-2 | liquid | Sigma-Aldrich | 59590 | ⩾97% |
| 4 | 1,2-ethanedithiol | 540-63-6 | liquid | Sigma-Aldrich | 02390 | ⩾98.0% |
| 5 | 1,3-propanedithiol | 109-80-8 | liquid | Sigma-Aldrich | P50609 | 99% |
| 6 | dimethyl sulfide | 75-18-3 | liquid | Sigma-Aldrich | 274380 | ⩾99% |
| 7 | methyl ethyl sulfide | 624-89-5 | liquid | Sigma-Aldrich | 238317 | 96% |
| 8 | bis(methylthio)methane | 1618-26-4 | liquid | Sigma-Aldrich | W387800 | ⩾99% |
| 9 | trimethylene sulfide | 287-27-4 | liquid | Macklin | T838543 | 98% |
| 10 | 1,3-dithiolane | 4829-04-3 | liquid | Macklin | D920796 | 97% |
| 11 | dimethyl disulfide | 624-92-0 | liquid | Macklin | M832301 | 98% |

298

**Table S2.** Reaction mechanism used to model the fate of $RO_2$• generated from •OH-initiated oxidation of DMS under NOx-free chamber conditions at 291 K (Exp. 10 in Table 1). The model was constructed as a simplified zero-dimensional box model to estimate the order of magnitude of $HO_2$• and $RO_2$• concentrations and to evaluate the relative timescales of $RO_2$• loss pathways. Numerical coefficients before products indicate stoichiometric coefficients or branching fractions used in the lumped mechanism.

| Reactant 1 | Reactant 2 | Product | Rate coefficient | Citation |
|---|---|---|---|---|
| $O_3$ | hv | $O(^1D)$ | 1.00E-05 | a |
| $O(^1D)$ | | 2OH | 2.00E+02 | a |
| DMS | OH | $RO_2$-MSP | 4.74E-12 | b |
| $RO_2$-MSP | $O_2$ | $RO_2$-HPMTF | 1.00E-01 | c |
| $RO_2$-MSP | $O_2$ | $RO_2$-SO | 1.00E-02 | d |
| $RO_2$-SO | $O_2$ | $RO_2$-SOO | 5.00E-02 | d |
| $RO_2$-SOO | $O_2$ | $RO_2$-$SO_2$ | 2.00E-01 | d |
| $RO_2$-MSP | $HO_2$ | P | 2.54E-11 | e |
| $RO_2$-HPMTF | $HO_2$ | P | 1.66E-11 | c |
| $RO_2$-SO | $HO_2$ | P | 2.54E-11 | e |
| $RO_2$-SOO | $HO_2$ | P | 2.54E-11 | e |
| $RO_2$-$SO_2$ | $HO_2$ | P | 2.54E-11 | e |
| $RO_2$-MSP | $RO_2$-MSP | 2RO | 4.00E-12 | f |
| $RO_2$-MSP | $RO_2$-HPMTF | 2RO | 2.28E-12 | f |
| $RO_2$-MSP | $RO_2$-SO | 2RO | 6.32E-12 | f |
| $RO_2$-MSP | $RO_2$-SOO | 2RO | 6.32E-12 | f |
| $RO_2$-MSP | $RO_2$-$SO_2$ | 2RO | 6.32E-12 | f |
| $RO_2$-HPMTF | $RO_2$-HPMTF | 2RO | 1.30E-12 | f |
| $RO_2$-HPMTF | $RO_2$-SO | 2RO | 3.61E-12 | f |
| $RO_2$-HPMTF | $RO_2$-SOO | 2RO | 3.61E-12 | f |
| $RO_2$-HPMTF | $RO_2$-$SO_2$ | 2RO | 3.61E-12 | f |
| $RO_2$-SO | $RO_2$-SO | 2RO | 1.00E-11 | f |
| $RO_2$-SO | $RO_2$-SOO | 2RO | 1.00E-11 | f |
| $RO_2$-SO | $RO_2$-$SO_2$ | 2RO | 1.00E-11 | f |
| $RO_2$-SOO | $RO_2$-SOO | 2RO | 1.00E-11 | f |
| $RO_2$-SOO | $RO_2$-$SO_2$ | 2RO | 1.00E-11 | f |
| $RO_2$-$SO_2$ | $RO_2$-$SO_2$ | 2RO | 1.00E-11 | f |
| RO | | $HO_2$ | 5.00E+00 | d |
| $HO_2$ | $HO_2$ | P | 3.00E-12 | g |

a PAM/OFR photochemical framework for OH generation using effective photolysis and O(1D)→OH conversion parameters (Lambe et al., 2011).

b Gas-phase OH abstraction of DMS forming $CH_3SCH_2OO•$, with the rate expression adopted from Saunders et al. (2003).

c First-order intramolecular H-shift isomerization of DMS-derived $CH_3SCH_2OO•$ to an isomerized $RO_2•$ pool associated with the HPMTF formation pathway. A rate coefficient of 0.1 $s^{-1}$ was adopted based on recent room-temperature DMS oxidation studies (Jernigan et al., 2022; Ye et al., 2022).

d Lumped first-order oxidation and RO• to $HO_2•$ conversion steps introduced to represent multistep oxidation and maintain $HO_x$ closure in the simplified chamber box model, following common box-model practice (Jacob et al., 2023; Lambe et al., 2011).

e Generic $RO_2•$ + $HO_2•$ termination rate expression adopted from the Master Chemical Mechanism (Jenkin et al., 2015).

f $RO_2•$ + $RO_2•$ termination parameterized using self-reaction rate constants and geometric-mean approximation for cross reactions, commonly used when explicit data are unavailable (Jacob et al., 2023; Jenkin et al., 2015).

g $HO_2•$ + $HO_2•$ termination rate from kinetic evaluations summarized by Atkinson et al. (2004).

Note: $RO_2$-MSP, $RO_2$-HPMTF, $RO_2$-SO, $RO_2$-SOO, and $RO_2$-$SO_2$ represent lumped classes of sulfur-containing organic peroxy radicals formed during the oxidation of DMS. $RO_2$-MSP corresponds to the initially formed carbon-centered peroxy radical, mainly $CH_3SCH_2OO•$, produced via H-abstraction from DMS. $RO_2$-HPMTF represents an isomerized $RO_2•$ pool formed following intramolecular H-shift of $RO_2$-MSP and is included to account for the HPMTF-related unimolecular pathway in a simplified manner. $RO_2$-SO, $RO_2$-SOO, and $RO_2$-$SO_2$ represent lumped sulfur-containing peroxy radicals with increasing sulfur oxidation states, intended to capture progressive sulfur oxidation without resolving individual molecular identities. P denotes a lumped pool of stable, non-radical oxidation products (e.g., ROOH, carbonyl-type products, and $H_2O_2$) that do not further participate in $HO_x$ or $RO_2•$ chemistry within the timescale of the model.

**Table S3.** Multi-sulfur products formed from the •OH-initiated oxidation of selected sulfur-VOCs and their volatility ($log_{10}C$ at 291 K) and yield (%).

| Species | sulfur-VOCs | Formulae | Multi-sulfur products | Charging method | $log_{10}C$(291K) | yield (%) | |
|---|---|---|---|---|---|---|---|
| Acyclic sulfide | dimethyl sulfide | $CH_3SCH_3$ | $C_2H_6O_4S_2$ | $C_2H_5O_4S_2^-$<br>$C_2H_6O_4S_2 \cdot NO_3^-$ | 2.27 | 3.286 | 4.249 |
| | | | $C_2H_6O_5S_2$ | $C_2H_5O_5S_2^-$ | 1.02 | 0.064 | |
| | | | $C_3H_8O_4S_2$ | $C_3H_7O_4S_2^-$ | 2.21 | 0.193 | |
| | | | $C_3H_8O_5S_2$ | $C_3H_8O_5S_2 \cdot HNO_3NO_3^-$ | 1.01 | 0.463 | |
| | | | $C_3H_8O_6S_2$ | $C_3H_7O_6S_2^-$ | -0.21 | 0.244 | |
| | methyl ethyl sulfide | $CH_3SCH_2CH_3$ | $C_2H_6O_4S_2$ | $C_2H_6O_4S_2 \cdot NO_3^-$ | 2.27 | 3.536 | 3.869 |
| | | | $C_2H_6O_5S_2$ | $C_2H_6O_5S_2 \cdot NO_3^-$ | 1.02 | 0.333 | |
| | bis(methylthio)methane | $CH_3SCH_2SCH_3$ | $C_2H_6O_4S_2$ | $C_2H_6O_4S_2 \cdot NO_3^-$ | 2.27 | 0.007 | 0.007 |
| Disulfide | dimethyl disulfide | $CH_3S_2CH_3$ | $C_2H_6O_4S_2$ | $C_2H_6O_4S_2 \cdot NO_3^-$ | 2.27 | 0.069 | 0.069 |
| Monothiol | 1-propanethiol | $CH_3(CH_2)_2SH$ | $C_6H_{14}O_3S_2$ | $C_6H_{14}O_3S_2 \cdot NO_3^-$ | 2.68 | 0.001 | 0.001 |
| | | | $C_6H_{14}O_4S_2$ | $C_6H_{14}O_4S_2 \cdot NO_3^-$ | 1.67 | 0.001 | |
| | 2-propanethiol | $(CH_3)_2CHSH$ | $C_6H_{14}O_3S_2$ | $C_6H_{14}O_3S_2 \cdot NO_3^-$ | 2.68 | 0.271 | 0.398 |
| | | | $C_6H_{14}O_4S_2$ | $C_6H_{14}O_4S_2 \cdot NO_3^-$ | 1.67 | 0.127 | |
| Dithiol | 1,2-ethanedithiol | $HS(CH_2)_2SH$ | $C_4H_{10}O_6S_2$ | $C_4H_9O_6S_2^-$ | -0.26 | 0.053 | 0.097 |
| | | | $C_4H_{10}O_8S_2$ | $C_4H_9O_8S_2^-$ | -3.94 | 0.019 | |
| | | | $C_4H_{10}O_9S_2$ | $C_4H_9O_9S_2^-$ | -2.70 | 0.024 | |
| | 1,3-propanedithiol | $HS(CH_2)_3SH$ | $C_6H_{14}O_4S_2$ | $C_6H_{14}O_4S_2 \cdot NO_3^-$ | 1.67 | 0.008 | 0.169 |
| | | | $C_6H_{14}O_7S_2$ | $C_6H_{13}O_7S_2^-$ | -1.65 | 0.027 | |
| | | | $C_6H_{14}O_8S_2$ | $C_6H_{13}O_8S_2^-$ | -2.82 | 0.032 | |
| | | | $C_6H_{14}O_9S_2$ | $C_6H_{13}O_9S_2^-$<br>$C_6H_{14}O_9S_2 \cdot NO_3^-$ | -4.01 | 0.088 | |
| | | | $C_6H_{14}O_{10}S_2$ | $C_6H_{14}O_{10}S_2 \cdot NO_3^-$ | -5.22 | 0.015 | |

| | | | | | | | |
|---|---|---|---|---|---|---|---|
| Cyclic sulfide | trimethylene sulfide | $C_3H_6S$ | $C_6H_{12}O_8S_2$ | $C_6H_{12}O_8S_2{\cdot}NO_3^-$ | -2.82 | 0.082 | 11.729 |
| | | | $C_6H_{12}O_9S_2$ | $C_6H_{11}O_9S_2^-$ | -4.01 | 0.230 | |
| | | | $C_6H_{12}O_{10}S_2$ | $C_6H_{12}O_{10}S_2{\cdot}NO_3^-$ | -5.22 | 0.208 | |
| | | | $C_6H_{14}O_7S_2$ | $C_6H_{14}O_7S_2{\cdot}NO_3^-$ | -1.65 | 1.572 | |
| | | | $C_6H_{14}O_8S_2$ | $C_6H_{13}O_8S_2^-$ | -2.82 | 0.243 | |
| | | | $C_6H_{14}O_9S_2$ | $C_6H_{13}O_9S_2^-$<br>$C_6H_{14}O_9S_2{\cdot}NO_3^-$ | -4.01 | 6.541 | |
| | | | $C_6H_{14}O_{10}S_2$ | $C_6H_{14}O_{10}S_2{\cdot}NO_3^-$ | -5.22 | 2.853 | |
| | 1,3-dithiolane | $C_3H_6S_2$ | $C_2H_6O_4S_2$ | $C_2H_5O_4S_2^-$<br>$C_2H_6O_4S_2{\cdot}NO_3^-$ | 2.27 | 0.191 | 0.925 |
| | | | $C_2H_6O_5S_2$ | $C_2H_5O_5S_2^-$<br>$C_2H_6O_5S_2{\cdot}NO_3^-$ | 1.02 | 0.033 | |
| | | | $C_2H_6O_6S_2$ | $C_2H_5O_6S_2^-$ | -0.25 | 0.047 | |
| | | | $C_3H_6O_4S_2$ | $C_3H_6O_4S_2{\cdot}NO_3^-$ | 2.21 | 0.035 | |
| | | | $C_3H_6O_5S_2$ | $C_3H_6O_5S_2{\cdot}NO_3^-$ | 1.01 | 0.065 | |
| | | | $C_3H_6O_6S_2$ | $C_3H_5O_6S_2^-$<br>$C_3H_6O_6S_2{\cdot}NO_3^-$ | -0.21 | 0.025 | |
| | | | $C_3H_6O_7S_2$ | $C_3H_6O_7S_2{\cdot}NO_3^-$ | -1.46 | 0.335 | |
| | | | $C_6H_{14}O_3S_2$ | $C_6H_{14}O_3S_2{\cdot}NO_3^-$ | 2.68 | 0.145 | |
| | | | $C_3H_8O_6S_2$ | $C_3H_8O_6S_2{\cdot}NO_3^-$ | -0.21 | 0.050 | |

331

**Table S4.** Fragment-to-parent signal ratios for representative sulfur-VOC standards during single-component Vocus-PTR-LToF-MS calibrations.

| Class | sulfur-VOC standard | Parent ion | Fragment-like ion | Fragment-to-parent ratio (%) |
|---|---|---|---|---|
| Monothiol | $CH_3CH_2SH$ | $C_2H_7S^+$ | $C_2H_6S^+$ | 2.0 |
| Dithiol | $HS(CH_2)_2SH$ | $C_2H_7S_2^+$ | $C_2H_6S_2^+$ | 10.0 |
| Acyclic sulfide | $CH_3SCH_3$ | $C_2H_7S^+$ | $C_2H_6S^+$ | 2.0 |
| Cyclic sulfide | $C_3H_6S$ | $C_3H_7S^+$ | $C_3H_6S^+$ | 2.0 |
| Disulfide | $CH_3S_2CH_3$ | $C_2H_7S_2^+$ | $C_2H_6S_2^+$ | 10.0 |

Note: Fragment-to-parent ratios were calculated from stable calibration plateaus during single-component Vocus-PTR-LToF-MS calibrations, excluding transient periods during concentration switching. Fragment-like ions were identified based on their synchronous temporal variation with the corresponding parent ions, as shown in Figure S14.

**Table S5.** Molecular formulas, sulfur atom numbers, and semi-quantitative apparent mixing ratios of sulfur-VOCs detected from freshwater algae emissions by Vocus-PTR-LToF-MS.

| Molecular formula | Molecular mass | Number of sulfur atoms | Apparent mixing ratio (ppbv) | Sensitivity (cps $pptv^{-1}$) |
|---|---|---|---|---|
| $CH_2S$ | 45.9877 | 1 | 4.087 | 0.92 |
| $CH_4S$ | 48.0033 | 1 | 11.773 | 0.61 |
| $C_2H_4S$ | 60.0033 | 1 | 3.573 | 0.92 |
| $C_2H_6S$ | 62.0190 | 1 | 8.595 | 0.92 |
| $C_3H_6S$ | 74.0190 | 1 | 0.693 | 0.92 |
| $C_3H_8S$ | 76.0346 | 1 | 1.188 | 0.57 |
| $CH_2S_2$ | 77.9597 | 2 | 0.081 | 0.82 |
| $CH_4S_2$ | 79.9754 | 2 | 0.044 | 0.82 |
| $C_2H_4S_2$ | 91.9754 | 2 | 0.186 | 0.82 |
| $C_2H_6S_2$ | 93.9910 | 2 | 0.324 | 0.82 |
| $C_3H_4S_2$ | 103.9754 | 2 | 0.248 | 0.82 |
| $C_3H_6S_2$ | 105.9910 | 2 | 0.688 | 0.82 |
| $C_3H_8S_2$ | 108.0067 | 2 | 0.305 | 0.82 |
| $C_5H_8S_2$ | 132.0067 | 2 | 0.063 | 0.82 |
| $C_6H_{14}S_2$ | 150.0536 | 2 | 0.783 | 0.82 |
| $C_2H_6S_3$ | 125.9631 | 3 | 0.067 | 0.82 |
| $C_3H_6S_3$ | 137.9631 | 3 | 0.062 | 0.82 |
| $C_4H_{10}S_3$ | 153.9944 | 3 | 0.495 | 0.82 |
| $C_2H_6S_4$ | 157.9352 | 4 | 0.008 | 0.82 |
| $C_3H_6S_4$ | 169.9352 | 4 | 0.006 | 0.82 |

Note: The listed entries represent sulfur-VOCs detected from freshwater algae emissions by Vocus-PTR-LToF-MS, rather than unambiguous isomer-specific compounds. Apparent mixing ratios were calculated using the sensitivity assignments listed in the last column; experimentally determined sensitivities were used where available, and proxy sensitivities were applied for formulas without compound-specific calibrations. Because Vocus-PTR-LToF-MS constrains molecular formulas rather than molecular structures and authentic standards were not available for all assigned formulas, the reported values should be interpreted as semi-quantitative apparent mixing ratios. Potential PTR ionization-related fragmentation was evaluated separately using single-component calibration experiments, as described in S4, Table S4, and Figure S14.

**Table S6.** Oxidation products formed from the •OH-initiated oxidation of freshwater algae-emitted VOCs and detected by nitrate-CI-LToF-MS.

| Species | Molecular formula | Molecular mass | Mass defect | Normalized value |
|---|---|---|---|---|
| Multi-sulfur products | $C_3H_8O_2S_2$ | 139.9965 | -0.00343 | 1.66E-03 |
| | $C_2H_6O_3S_2$ | 141.9758 | -0.02416 | 1.36E-04 |
| | $C_4H_{10}O_2S_2$ | 154.0122 | 0.01222 | 1.71E-05 |
| | $C_2H_4O_4S_2$ | 155.9551 | -0.04490 | 9.15E-06 |
| | $C_3H_8O_3S_2$ | 155.9914 | -0.00851 | 3.82E-05 |
| | $C_3H_8O_2S_3$ | 171.9686 | -0.03136 | 1.23E-04 |
| | $C_6H_{12}O_2S_2$ | 180.0278 | 0.02787 | 4.58E-05 |
| | $C_6H_{14}O_2S_2$ | 182.0435 | 0.04352 | 1.68E-05 |
| | $C_3H_8O_3S_3$ | 187.9635 | -0.03644 | 1.09E-05 |
| | $C_2H_6O_7S_2$ | 205.9554 | -0.04451 | 7.61E-06 |
| | $C_{10}H_{22}O_3S_3$ | 286.0731 | 0.07311 | 3.57E-05 |
| Mono-sulfur products | $CH_4O_3S$ | 95.9881 | -0.01188 | 2.42E-02 |
| | $C_2H_4O_3S$ | 107.9881 | -0.01188 | 6.54E-05 |
| | $CH_2O_4S$ | 109.9673 | -0.03262 | 1.69E-05 |
| | $CH_4O_4S$ | 111.9830 | -0.01697 | 2.12E-04 |
| | $C_3H_6O_3S$ | 122.0037 | 0.00377 | 6.85E-05 |
| | $C_3H_8O_3S$ | 124.0194 | 0.01941 | 4.01E-04 |
| | $C_3H_6O_4S$ | 137.9986 | -0.00132 | 6.21E-06 |
| | $C_2H_4O_5S$ | 139.9779 | -0.02206 | 1.13E-05 |
| | $C_3H_8O_4S$ | 140.0143 | 0.01433 | 5.95E-05 |
| | $C_3H_4O_5S$ | 151.9779 | -0.02206 | 1.10E-05 |
| | $C_3H_6O_5S$ | 153.9935 | -0.00641 | 2.00E-05 |
| | $C_2H_4O_6S$ | 155.9728 | -0.02714 | 1.70E-05 |
| | $C_3H_8O_5S$ | 156.0092 | 0.00924 | 9.78E-06 |
| | $C_4H_6O_6S$ | 181.9885 | -0.01149 | 4.22E-06 |
| | $C_7H_{12}O_5S$ | 208.0405 | 0.04054 | 6.29E-06 |
| | $C_6H_{12}O_7S$ | 228.0303 | 0.03037 | 4.18E-06 |
| | $C_9H_{12}O_5S$ | 232.0405 | 0.04054 | 1.93E-04 |
| | $C_{12}H_{12}O_3S$ | 236.0507 | 0.05071 | 1.19E-04 |
| | $C_7H_{10}O_7S$ | 238.0147 | 0.01472 | 8.62E-06 |
| | $C_{12}H_{14}O_3S$ | 238.0663 | 0.06636 | 2.22E-04 |
| | $C_{13}H_{14}O_3S$ | 250.0663 | 0.06636 | 2.68E-04 |
| | $C_{12}H_{14}O_4S$ | 254.0612 | 0.06128 | 1.52E-04 |
| | $C_{13}H_{18}O_3S$ | 254.0976 | 0.09766 | 2.81E-04 |
| | $C_{13}H_{14}O_4S$ | 266.0612 | 0.06128 | 7.47E-05 |
| | $C_{13}H_{16}O_4S$ | 268.0769 | 0.07693 | 7.64E-04 |
| | $C_9H_{18}O_7S$ | 270.0773 | 0.07732 | 1.61E-05 |

| | | | | |
|---|---|---|---|---|
| Inorganic sulfur products and clusters | $H_2SO_3$ | 81.9724 | -0.02754 | 3.53E-05 |
| | $H_2SO_4$ | 97.9673 | -0.03262 | 4.40E-03 |
| | $H_2SO_5$ | 113.9622 | -0.03771 | 1.78E-04 |
| | $(CH_4O_3S)_2$ | 191.9762 | -0.02377 | 1.82E-04 |
| | $H_2SO_4 \cdot CH_4O_3S$ | 193.9554 | -0.04451 | 1.50E-03 |
| | $(H_2SO_4)_2$ | 195.9347 | -0.06524 | 2.24E-04 |
| Other products | $C_2H_4O_3$ | 76.0160 | 0.01604 | 8.44E-06 |
| | $C_2H_2O_4$ | 89.9953 | -0.00469 | 5.14E-06 |
| | $C_3H_6O_3$ | 90.0316 | 0.03169 | 2.18E-06 |
| | $C_2H_4O_4$ | 92.0109 | 0.01096 | 1.18E-06 |
| | $C_2H_6O_4$ | 94.0266 | 0.02661 | 3.93E-06 |
| | $C_4H_4O_3$ | 100.0160 | 0.01604 | 4.62E-06 |
| | $C_3H_2O_4$ | 101.9953 | -0.00469 | 2.71E-05 |
| | $C_4H_6O_3$ | 102.0316 | 0.03169 | 5.87E-06 |
| | $C_3H_5NO_3$ | 103.0269 | 0.02694 | 8.31E-06 |
| | $C_3H_4O_4$ | 104.0109 | 0.01096 | 1.03E-04 |
| | $C_4H_8O_3$ | 104.0473 | 0.04734 | 1.07E-06 |
| | $C_5H_4O_3$ | 112.0160 | 0.01604 | 1.50E-06 |
| | $C_4H_4O_4$ | 116.0109 | 0.01096 | 5.14E-06 |
| | $C_3H_4N_2O_3$ | 116.0221 | 0.02219 | 1.10E-04 |
| | $C_5H_8O_3$ | 116.0473 | 0.04734 | 4.85E-06 |
| | $C_4H_7NO_3$ | 117.0425 | 0.04259 | 1.61E-06 |
| | $C_2H_2N_2O_4$ | 118.0014 | 0.00146 | 2.72E-06 |
| | $C_4H_6O_4$ | 118.0266 | 0.02661 | 3.39E-06 |
| | $C_3H_4O_5$ | 120.0058 | 0.00587 | 1.94E-05 |
| | $C_3H_6O_5$ | 122.0215 | 0.02152 | 1.04E-05 |
| | $C_3H_8O_5$ | 124.0371 | 0.03717 | 7.38E-04 |
| | $C_5H_7NO_3$ | 129.0425 | 0.04259 | 4.59E-06 |
| | $C_5H_6O_4$ | 130.0266 | 0.02661 | 3.42E-05 |
| | $C_6H_{10}O_3$ | 130.0629 | 0.06299 | 2.14E-06 |
| | $C_5H_9NO_3$ | 131.0582 | 0.05824 | 3.55E-06 |
| | $C_4H_4O_5$ | 132.0058 | 0.00587 | 3.08E-06 |
| | $C_5H_8O_4$ | 132.0422 | 0.04226 | 8.71E-06 |
| | $C_4H_6O_5$ | 134.0215 | 0.02152 | 2.16E-06 |
| | $C_4H_8O_5$ | 136.0371 | 0.03717 | 4.89E-05 |
| | $C_7H_6O_3$ | 138.0316 | 0.03169 | 9.26E-05 |
| | $C_6H_6O_4$ | 142.0266 | 0.02661 | 2.17E-05 |
| | $C_7H_{10}O_3$ | 142.0629 | 0.06299 | 1.39E-05 |
| | $C_6H_8O_4$ | 144.0422 | 0.04226 | 7.22E-06 |
| | $C_5H_6O_5$ | 146.0215 | 0.02152 | 2.67E-06 |
| | $C_5H_8O_5$ | 148.0371 | 0.03717 | 2.18E-05 |
| | $C_7H_6O_4$ | 154.0266 | 0.02661 | 1.03E-05 |

| | | | | |
|---|---|---|---|---|
| | $C_6H_4O_5$ | 156.0058 | 0.00587 | 6.71E-06 |
| | $C_7H_8O_4$ | 156.0422 | 0.04226 | 5.65E-06 |
| | $C_6H_6O_5$ | 158.0215 | 0.02152 | 1.43E-05 |
| | $C_7H_{10}O_4$ | 158.0579 | 0.05791 | 9.18E-06 |
| | $C_6H_8O_5$ | 160.0371 | 0.03717 | 1.03E-05 |
| | $C_5H_6O_6$ | 162.0164 | 0.01644 | 1.27E-05 |
| | $C_7H_{14}O_4$ | 162.0892 | 0.08921 | 2.90E-06 |
| | $C_6H_{12}O_5$ | 164.0684 | 0.06847 | 2.20E-05 |
| | $C_8H_8O_4$ | 168.0422 | 0.04226 | 3.15E-06 |
| | $C_7H_6O_5$ | 170.0215 | 0.02152 | 1.93E-05 |
| | $C_8H_{10}O_4$ | 170.0579 | 0.05791 | 1.11E-05 |
| | $C_7H_8O_5$ | 172.0371 | 0.03717 | 1.56E-06 |
| | $C_8H_{12}O_4$ | 172.0735 | 0.07356 | 2.04E-05 |
| | $C_8H_{14}O_4$ | 174.0892 | 0.08921 | 6.53E-05 |
| | $C_8H_6O_5$ | 182.0215 | 0.02152 | 1.06E-05 |
| | $C_6H_6O_7$ | 190.0113 | 0.01135 | 1.75E-05 |
| | $C_8H_{14}O_5$ | 190.0841 | 0.08412 | 3.53E-05 |
| | $C_6H_{10}O_7$ | 194.0426 | 0.04265 | 8.42E-05 |
| | $C_{10}H_{14}O_4$ | 198.0892 | 0.08921 | 7.19E-06 |
| | $C_8H_8O_6$ | 200.0320 | 0.03209 | 3.35E-05 |
| | $C_8H_{10}O_6$ | 202.0477 | 0.04774 | 1.71E-04 |
| | $C_8H_{12}O_6$ | 204.0633 | 0.06339 | 2.93E-04 |
| | $C_9H_{16}O_5$ | 204.0997 | 0.09977 | 3.93E-05 |
| | $C_7H_{10}O_7$ | 206.0426 | 0.04265 | 4.72E-05 |
| | $C_{11}H_{10}O_4$ | 206.0579 | 0.05791 | 1.88E-06 |
| | $C_8H_{14}O_6$ | 206.0790 | 0.07904 | 8.90E-05 |
| | $C_9H_{18}O_5$ | 206.1154 | 0.11542 | 5.79E-05 |
| | $C_7H_{12}O_8$ | 224.0532 | 0.05322 | 4.13E-05 |
| | $C_{12}H_{10}O_7$ | 266.0426 | 0.04265 | 3.78E-05 |
| | $C_{10}H_{10}O_9$ | 274.0324 | 0.03248 | 7.89E-06 |
| | $C_{12}H_{20}O_7$ | 276.1209 | 0.12090 | 4.29E-06 |

353

**References**


Atkinson, R., Baulch, D. L., Cox, R. A., Crowley, J. N., Hampson, R. F., Hynes, R. G., Jenkin, M. E., Rossi, M. J., and Troe, J.: Evaluated kinetic and photochemical data for atmospheric chemistry: Volume I - gas phase reactions of $O_x$, $HO_x$, $NO_x$ and $SO_x$ species, Atmos. Chem. Phys., 4, 1461–1738, https://doi.org/10.5194/acp-4-1461-2004, 2004.

Berndt, T., Scholz, W., Mentler, B., Fischer, L., Hoffmann, E. H., Tilgner, A., Hyttinen, N., Prisle, N. L., Hansel, A., and Herrmann, H.: Fast Peroxy Radical Isomerization and OH Recycling in the Reaction of OH Radicals with Dimethyl Sulfide, J. Phys. Chem. Lett., 10, 6478–6483, https://doi.org/10.1021/acs.jpclett.9b02567, 2019.

Hansel, A., Jordan, A., Holzinger, R., Prazeller, P., Vogel, W., and Lindinger, W.: Proton transfer reaction mass spectrometry: on-line trace gas analysis at the ppb level, Int. J. Mass Spectrom. Ion Process., 149, 609–619, https://doi.org/10.1016/0168-1176(95)04294-u, 1995.

Iida, Y., Obi, K., and Imamura, T.: Rate Constant for the Reaction of OH Radicals with Isoprene at 298±2 K, Chem. Lett., 31, 792–793, https://doi.org/10.1246/cl.2002.792, 2002.

IUPAC: Evaluated kinetic and photochemical data for atmospheric chemistry, IUPAC, 2021.

Jacob, L. S. D., Giorio, C., and Archibald, A. T.: Extension, development, and evaluation of the representation of the OH-initiated dimethyl sulfide (DMS) oxidation mechanism in the Master Chemical Mechanism (MCM) v3.3.1 framework, Atmos. Chem. Phys., 24, 3329–3347, https://doi.org/10.5194/acp-24-3329-2024, 2023.

Jenkin, M. E., Young, J. C., and Rickard, A. R.: The MCM v3.3.1 degradation scheme for isoprene, Atmos. Chem. Phys., 15, 11433–11459, https://doi.org/10.5194/acp-15-11433-2015, 2015.

Jernigan, C. M., Fite, C. H., Vereecken, L., Berkelhammer, M. B., Rollins, A. W., Rickly, P. S., Novelli, A., Taraborrelli, D., Holmes, C. D., and Bertram, T. H.: Efficient Production of Carbonyl Sulfide in the Low-NOx Oxidation of Dimethyl Sulfide, Geophys. Res. Lett., 49, https://doi.org/10.1029/2021gl096838, 2022.

Krechmer, J., Lopez-Hilfiker, F., Koss, A., Hutterli, M., Stoermer, C., Deming, B., Kimmel, J., Warneke, C., Holzinger, R., Jayne, J., Worsnop, D., Fuhrer, K., Gonin, M., and Gouw, J. de: Evaluation of a New Reagent-Ion Source and Focusing Ion–Molecule Reactor for Use in Proton-Transfer-Reaction Mass Spectrometry, Anal. Chem., 90, 12011–12018, https://doi.org/10.1021/acs.analchem.8b02641, 2018.

Lambe, A. T., Ahern, A. T., Williams, L. R., Slowik, J. G., Wong, J. P. S., Abbatt, J. P. D., Brune, W. H., Ng, N. L., Wright, J. P., Croasdale, D. R., Worsnop, D. R., Davidovits, P., and Onasch, T. B.: Characterization of aerosol photooxidation flow reactors: heterogeneous oxidation, secondary organic aerosol formation and cloud condensation nuclei activity measurements, Atmos. Meas. Tech., 4, 445–461, https://doi.org/10.5194/amt-4-445-2011, 2011.

Lightfoot, P. D., Cox, R. A., Crowley, J. N., Destriau, M., Hayman, G. D., Jenkin, M. E., Moortgat, G. K., and Zabel, F.: Organic peroxy radicals: Kinetics, spectroscopy and tropospheric chemistry, Atmos. Environ. Part A Gen. Top., 26, 1805–1961, https://doi.org/10.1016/0960-1686(92)90423-i, 1992.

Medeiros, D. J., Blitz, M. A., James, L., Speak, T. H., and Seakins, P. W.: Kinetics of the Reaction of OH with Isoprene over a Wide Range of Temperature and Pressure Including Direct Observation of Equilibrium with the OH Adducts, J. Phys. Chem. A, 122, 7239–7255, https://doi.org/10.1021/acs.jpca.8b04829, 2018.

Orlando, J. J. and Tyndall, G. S.: Laboratory studies of organic peroxy radical chemistry: an overview with emphasis on recent issues of atmospheric significance, Chem. Soc. Rev., 41, 6294, https://doi.org/10.1039/c2cs35166h, 2012.

Saunders, S. M., Jenkin, M. E., Derwent, R. G., and Pilling, M. J.: Protocol for the development of the Master Chemical Mechanism, MCM v3 (Part A): tropospheric degradation of non-aromatic volatile organic compounds, Atmos. Chem. Phys., 3, 161–180, https://doi.org/10.5194/acp-3-161-2003, 2003.

Ye, Q., Goss, M. B., Krechmer, J. E., Majluf, F., Zaytsev, A., Li, Y., Roscioli, J. R., Canagaratna, M., Keutsch, F. N., Heald, C. L., and Kroll, J. H.: Product distribution, kinetics, and aerosol formation from the OH oxidation of dimethyl sulfide under different RO2 regimes, Atmos. Chem. Phys., 22, 16003–16015, https://doi.org/10.5194/acp-22-16003-2022, 2022.

Yuan, B., Koss, A. R., Warneke, C., Coggon, M., Sekimoto, K., and Gouw, J. A. de: Proton-Transfer-Reaction Mass Spectrometry: Applications in Atmospheric Sciences, Chem. Rev., 117, 13187–13229, https://doi.org/10.1021/acs.chemrev.7b00325, 2017.